# Application of TOPSAR and Polarimetric SAR for Geological Mapping within north western Tasmania

Dr Rob Hewson
RMIT University

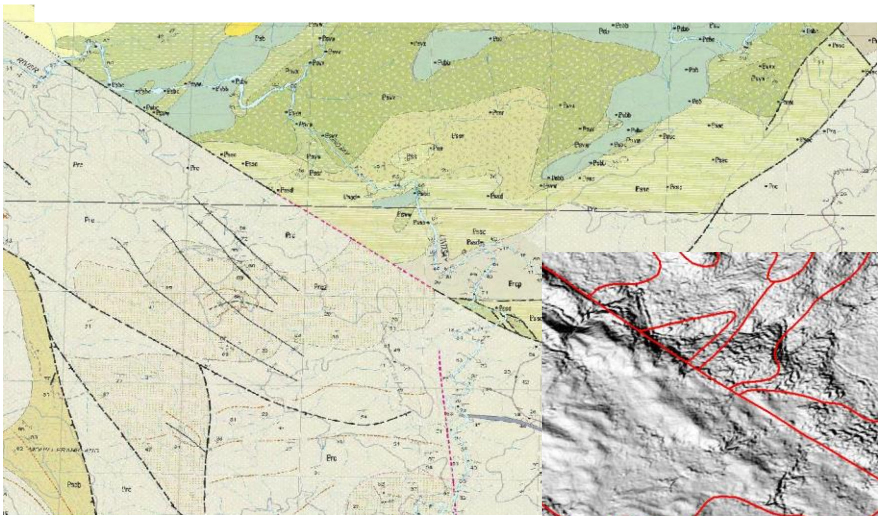

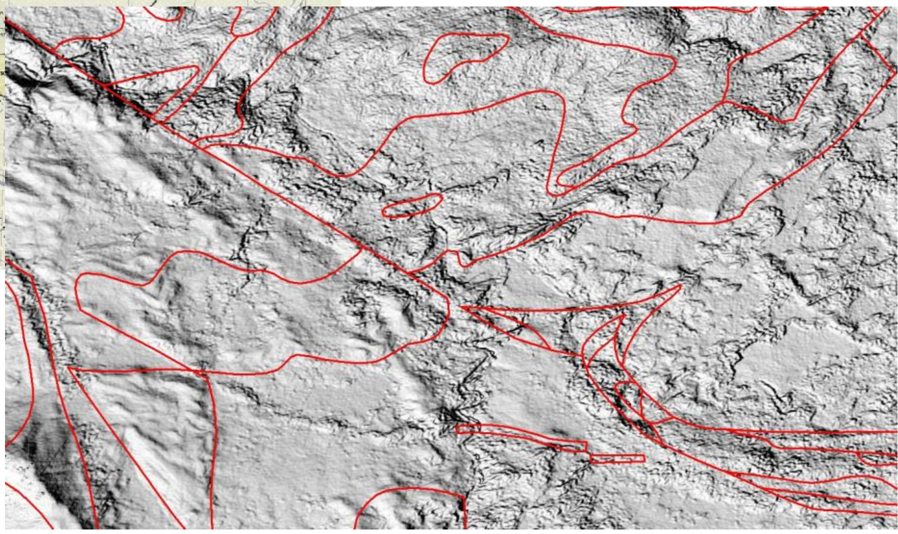

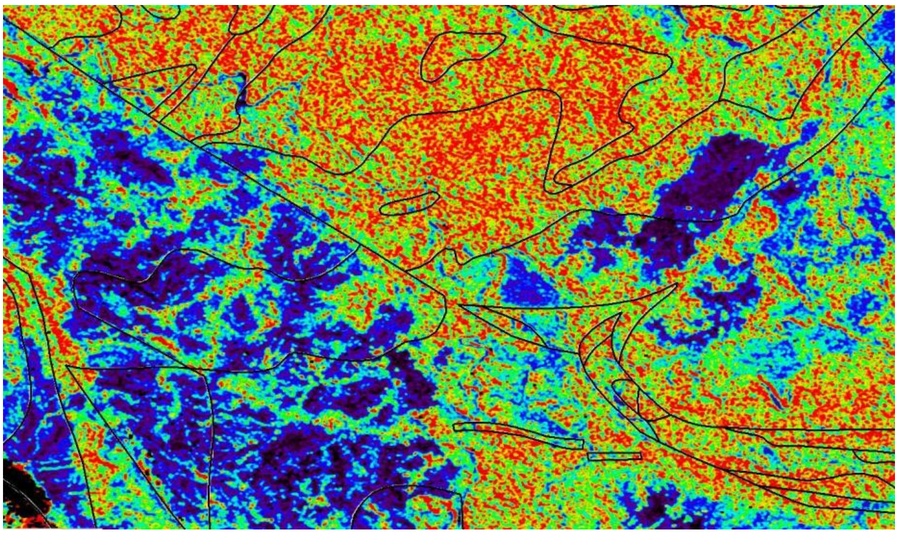

**May 2015**

# Table of Contents

# Table of Figures

## Table of Tables

# 1 Introduction

## 1.1 Polarimetric radar and TOPSAR basics

Radar remote sensing generates imagery that characterises some of the physical properties (morphology, roughness, dielectric properties and geometric shapes) of the ground surface, including its cover (*e.g.* vegetation) and near-surface volume (*e.g.* rock outcrops and regolith layers) (Raney, 1998). It differs from optical or thermal remote sensing in its use of active microwave electromagnetic signals (Figure 1) and interpretation of their backscattered return for electric field strength and polarisation. The operation of radar from either a satellite or airborne platform involves a side looking pulse of microwave radiation transmitted perpendicular to the flight (or orbit) “range’ direction and observed by a receiver antenna (Figure 2). A variation of radar systems known as Synthetic Aperture Radar (SAR) optimises the spatial resolution using the Doppler return of the signal along the azimuth flight path of the platform.

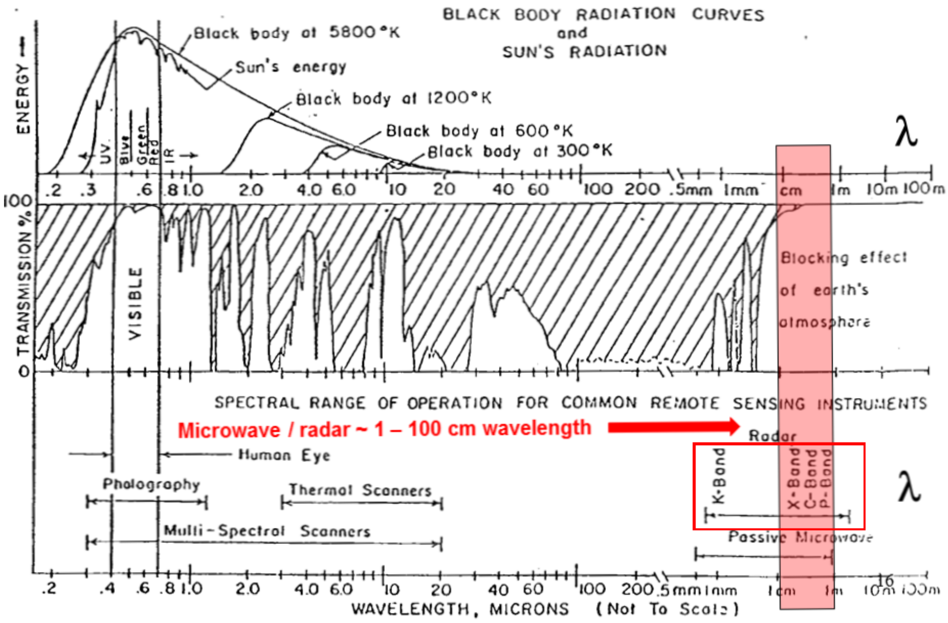


Figure 1 Remote sensing regions including radar in relation to the electromagnetic spectrum. The relative wavelengths of the active radar bands K, X, C and P are shown. Note L band has a wavelength between C and P bands.

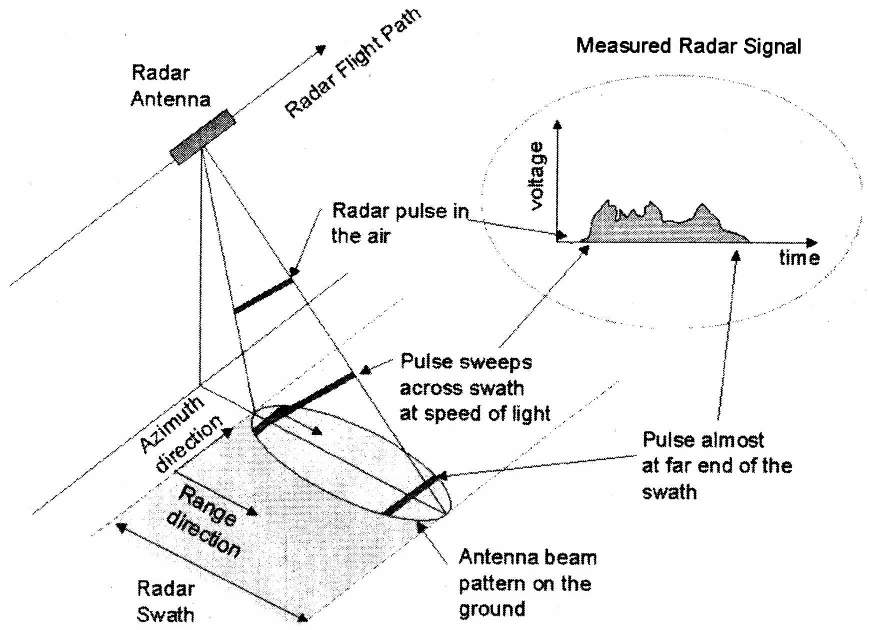


Figure 2 Operation of a radar system

The application radar for the extraction of geological information relies on the surface geometry and its contrasting dielectric properties, typically related to moisture content or mineral composition (Ford, 1998). The geological interpretation of image enhancements are particularly suited to landform analysis from which geomorphological and geological structural interpretation can be made (Tapley, 2002). The radar technique provides its own illumination enabling observations to be independent of cloud cover, light rain, smoke haze and solar illumination, thus allowing all-time observation through all seasons and in all climatic regions. An important capability of radar is the ability to select the illumination geometry, that is, the incidence and azimuth angles, to highlight geological structure and other diagnostic properties of the terrain. Case studies describing SAR radar surveys within densely forested areas of Indonesia and Papua New Guinea have still shown its ability to map both structural features and erosional characteristics of the underlying rocks (Ford, 1998).

Radar technologies such as NASA's multi wavelength polarimetric AIRSAR systems (Lou, 2002; http://airsar.jpl.nasa.gov/) include the include the longer wavelength P (68 cm) and L (25 cm) bands. AIRSAR has the potential capability to measure backscattered signal returns beneath forest canopies related to surface rock outcrops and sub surface regolith (Ford - Henderson and Lewis, 1998; Evans *et al*., 1988). The AIRSAR system incorporates multi-polarimetric combinations of transmitted horizontal (H) or vertical (V) electric field signals,

and the detection of returning horizontal (H) or vertical (V) electric field returned backscatter. This facilitates the modelling of surface and volume radar scattering associated with vegetation and/or regolith (Figure 3). For example, surface scattering is more likely associated with like-polarized transmitted and returned signals (*e.g.* HH or VV) while volume scattering is associated with cross-polarized transmitted and returned signals (*e.g.* HV) (Figure 3). A complete multi -wavelength -polarimetric AIRSAR data set provides all these combinations for C, L and P bands including a total power backscatter measurement (TP) Note that a HV return is assumed to be equivalent to VH polarisation.
E.g. C-HH, C-VV, C-HV, C-TP, L-HH, L-VV, L-HV, L-TP, P-HH, P-VV, P-HV, P-TP
Generally the bands associated with longer AIRSAR radar wavelengths, P and to a lesser extent L, measure more backscatter from beneath the vegetation canopy and ground surface and or regolith (Tapley, 2002). In particular, the HV polarization for P (P-HV) band provides the best indication of volume scattering from the shallow subsurface associated with the rock outcrops and regolith. In forested environments, HH polarisation signals potentially suffer less attenuation from the vertically aligned tree trunks and are more likely to provide information about the physical characteristics of the underlying ground-surface (Tapley, 2002). The cross-polarized HV scattering bands are less dependent on incidence angle, varying perpendicular across the flight line, than the co-polarized (HH and VV) backscatter (Tapley, 2002). Consequently HV returns are also less sensitive to variations in terrain slope. Geobotanical relationships, between geological units and vegetation species or forest type are potentially highlighted by the VV polarisation data which is associated with increased interaction with the vegetation and tree trunks (Tapley, 2002).

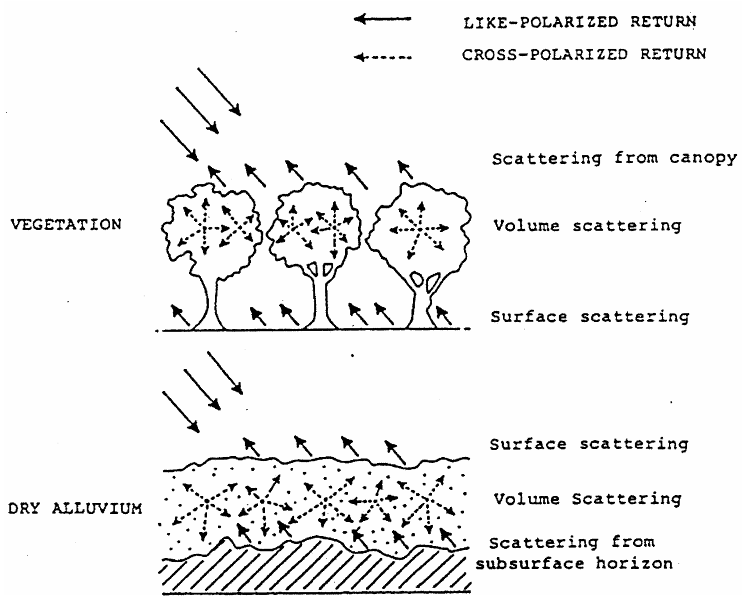


Figure 3 Volume and surface scattering modes for transmitted and returned radar.

In addition, AIRSAR's C band (5.7 cm) is utilised within its TOPSAR system for interferometric topographic mapping (Zebker *et al.*, 1992; Madsen *et al*, 1993) (Figure 4 a & b). Observing the returned radar backscatter of the C band signal with two detectors, A1 and A2 (Figure 4a) enables the determination of height, h, for each scanned pixel, z(x) (Figure 4b). As TOPSAR uses the C-VV wavelength and polarisation, its returned backscatter signals are typically biased by the vegetation canopy.

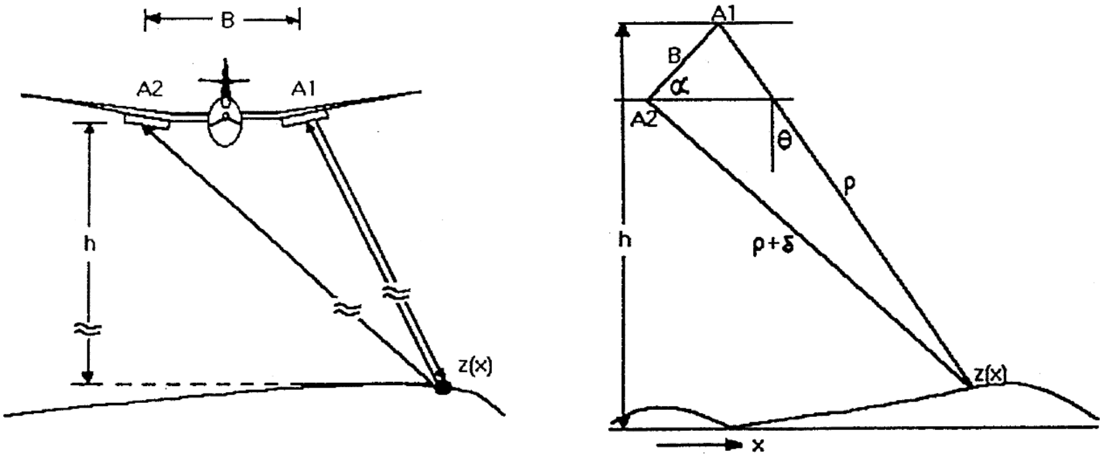


Figure 4 a) Schematic diagram of TOPSAR operation, and b) its corresponding geometry.

## 1.2 Objectives

The aim of this report is to describe the processing and preliminary geological interpretation of TOPSAR acquired by Mineral Resources Tasmania from three flight lines in north western Tasmania during the PACRIM 2 Campaign, August 2000 (Figure 5). As part of this study, the quality control issues of the resulting Digital Elevation Model (DEM) and its comparisons with supplied LiDAR, SRTM 25 metre and 1:25000 Photogrammetric DEM products are examined. The fully polarimetric AIRSAR/POLSAR Mt Read data, acquired in 1993 (Figure 5), was not able to be processed with the current ENVI™ software (http://www.exelisvis.com/ProductsServices/ENVIProducts/ENVI.aspx). Its data format appears to be in an atypical format and its processing and interpretation awaits an update by the suppliers of ENVI™ .

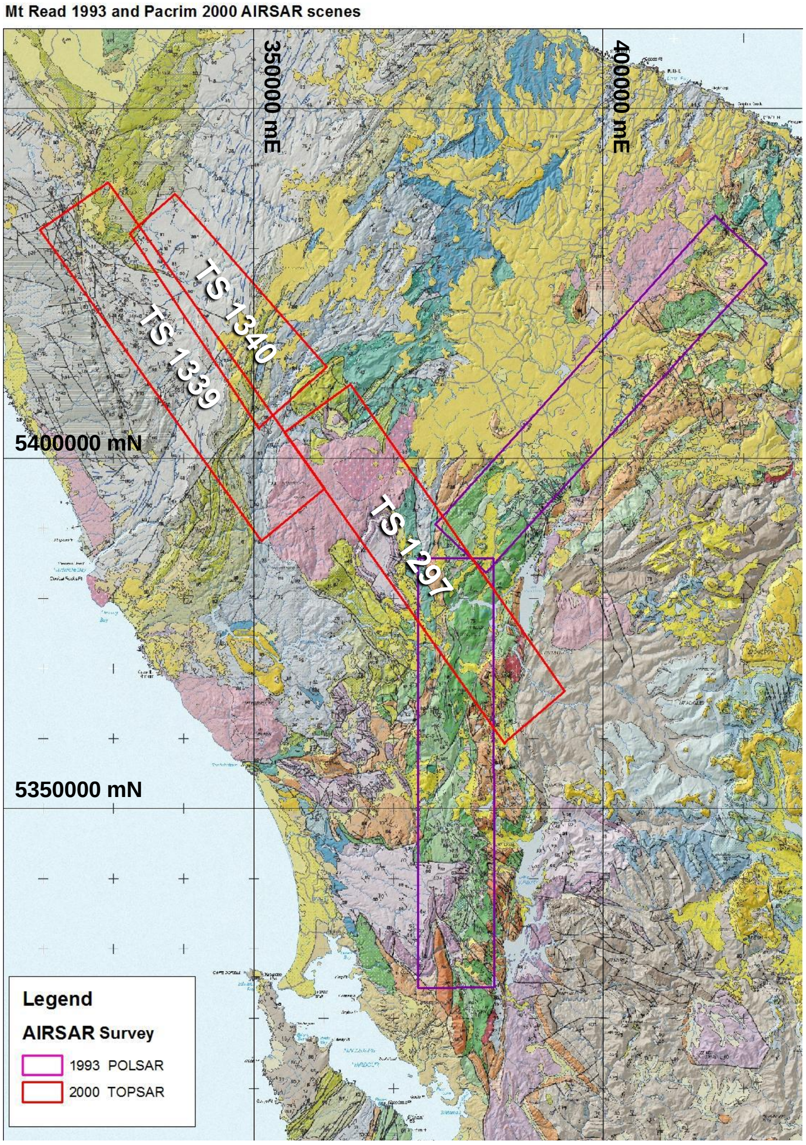


Figure 5 Location of 1993 POLSAR (AIRSAR) and 2000 PACRIM TOPSAR within north western Tasmania.

# 2 Datasets, processing and quality control issues

## 2.1 TOPSAR Polarimetric

The PACRIM 2 TOPSAR data comprised nine channels comprising C-VV, L-HH, L-VV, L-HV, L-TP, P-HH, P-VV, P-HV, and P-TP. Three flight lines of TOPSAR imagery, TS1297, TS1340 and TS1339 were acquired of approximately 60 x 10 km, 60 x 10 km and 30 x 10 km image areas respectively (Figure 5). These were imported into ENVI™ software which facilitates the synthesis of the multiple wavelengths and polarisations from the Stokes Matrix Compression format (http://airsar.jpl.nasa.gov/documents/dataformat.htm). The nine channel imagery was then registered in a three stage process :

1) polarimetric TOPSAR imagery were registered using the WGS 84 geographic coordinates within the supplied header information for the corners (Appendix 1);
2) the WGS 84 projected imagery was converted to GDA94 MGA Zone 55S Easting and Northing coordinate projection;
3) The GDA94 MGA Zone 55 was registered using 20 to 30 ground control points identified by features (watercourse/road intersections, dam walls, mountain peaks etc) identified on supplied MRT 1:25000 topographic maps, SPOT imagery and 1:25,000, and 1:25000 Photogrammetric and SRTM 25 metre DEMs (Figure A1, Appendix 1).

The resulting GDA94 MGA Zone 55 polarimetric TOPSAR imagery was imported into ERDAS ERMapper™ (http://erdas-er-mapper.software.informer.com/) for integration and comparison with supplied MRT datasets. Some issues of systematic spatial noise were apparent and likely to have resulted from AIRSAR system and aircraft electronics (Tapley, 2002). Two dimensional (2D) Fast Fourier Transform (FFT) 2D band cut filtering was attempted using ENVI™ however difficulty was encountered in the exclusion of the systematic spatial frequency noise while not introducing noise from the user defined band cuts. As a consequence, no FFT filtering was applied to this TOPSAR imagery. However a more serious noise issue was apparent from radar "speckle", associated with inherent random and multiplicative returning coherent backscatter (Tapley, 2002). Various adaptive filtering techniques using both ENVI™ and ERDAS ERMapper™ software including Median, Gamma, Froist and Lee filters (Lopes *et al*., 1990). The standard Lee filter (Lee, 1980) available using ERDAS ERMapper™ was found to give the best result in reducing the speckle for this AIRSAR/TOPSAR imagery. This operation of this filter is based on the probability of a Gaussian distribution where 95.5% of random samples are assumed to be within a 2 standard deviation (2 sigma) range. This noise suppression filter replaces the pixel of interest with the average of all DN values within a 5 x 5 pixel sample moving window that fall within the designated range (ERDAS, 1999)

## 2.2 TOPSAR DEM

The PACRIM 2 TOPSAR DEM data comprised four bands including the C-VV polarised band, the correlation information (DEM accuracy estimate), the incidence angle (degrees) of the radar signal and the calculated topographic DEM. The conversion from the supplied TOPSAR data format into these four parameters was done using ENVI™. Missing radar returns from radar shadows produced by the topography were replaced using standard surface fitting techniques available with ENVI™ although the interpolation was still apparent in some areas of these TOPSAR DEM imagery. The resulting four parameters associated with the C band derived DEM comprised identical number of pixel and line samples as the TOPSAR polarimetric file for each flight line and WGS 84 geographic coordinates within the supplied header information (Appendix 1). Consequently the same registration procedure listed in Section 2.1 was followed to generate equivalent GDA94 MGA Zone 55S imagery for the three flight lines.

## 2.3 Issues affecting radar interpretation and quality control

### 2.3.1 Incident angle

The sensitivity of a radar systems response to the geometry of its operation and the acquisition of returning backscatter is illustrated by Figures 6 and 7. In particular Figure 6 shows the issue of layover distorting the dimensions of the topographic slopes for large radar depression angles, while radar shadowing can be present for shallow depression angles. Typically the AIRSAR/TOPSAR system describe their acquisition specifications in terms of look angle, which is related to the depression (*e.g*. = 90 – look angle degrees) and incident angles as shown in Figure 7a). In a flat ground surface situation, the look angle and incident angles are equal (Figure 7a) however the local incident angle can be significantly affected by local topography (Figure 7b). When the local incidence angle is smaller than the local slope angle layover effects and distortion will be apparent (Raney, 1998).

The high spatial sampling resolution of 5 metres acquired by the AIRSAR/TOPSAR imagery makes the local incident angle particularly important in the steeply dipping relief of western Tasmania. The range of look angles measured by the AIRSAR/TOPSAR PACRIM2 surveys varied between approximately 25 and 64 degrees. In general the larger look angles acquired by AIRSAR/TOPSAR at the furthest extent of the swath or range (*e.g.* 50-64 degrees) will generally accentuate geomorphic and structural features related to topographic relief and outcrop by their apparent shadowing effect. At shallower look angles (*e.g.* 25-35 degrees) a greater chance of spatial distortion and layover effects is also possible, depending on the local relief.

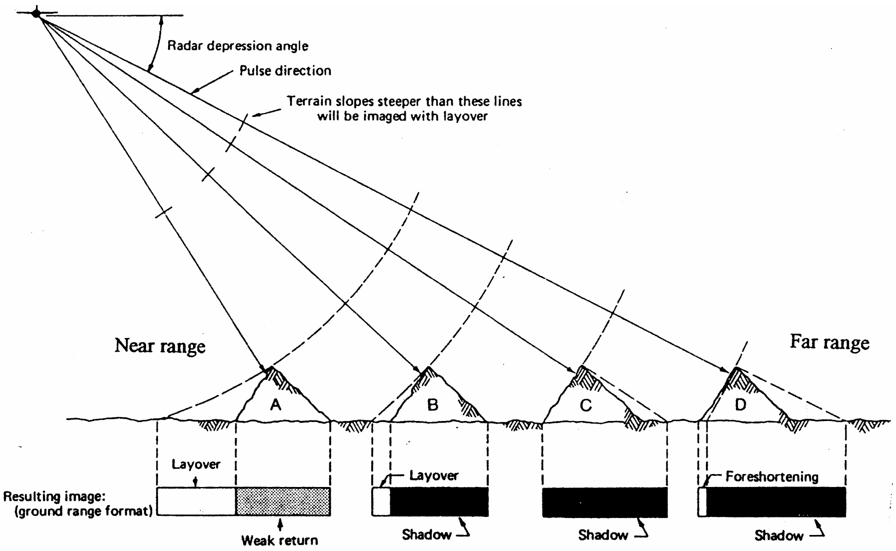


Figure 6 Schematic diagram illustrating the interaction between topography and the radar depression angle on the resulting radar image effects of layover and shadowing (Elachi & Van Zyl, 2006).

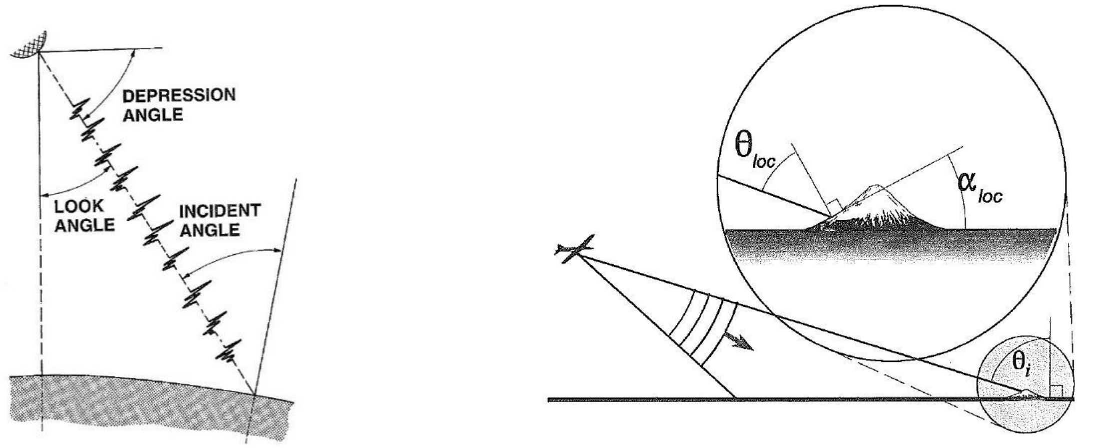


a) b)

Figure 7 a) Relationship between look angle, depression angle and incident angle assuming a relatively flat ground surface (Ford, 1998); b) Schematic diagram illustrating local incident angle $\theta_{loc}$ and the average incident angle $\theta_i$ resulting from local slope angle $\alpha_{loc}$ (Raney, 1998).

### 2.3.2 Surface roughness

In general radar backscatter increases with increasing surface roughness depending on the radar wavelength (Raney, 1998). Geological applications of AIRSAR/TOPSAR utilise these effects of the differing responses to surface roughness by observing the response to the three different band wavelengths. In particular, the surface roughness properties of the rock outcrops and regolith, will generate variable amounts of diffuse backscatter according to the wavelength of the radar pulse and its incident (local) angle. Surface roughness is typically measured in terms of root mean square (rms) measures varying from millimetres , centimetres to metres for very rocky terrain. Quantitatively, a surface is considered definitely "rough" (*e.g*. generating a high backscatter response) if :

$$h > \lambda / (4.4 \cos \theta) \qquad (1)$$

where h : rms height, λ : radar wavelength, and θ : incident angle (Ford, 1998). Alternatively a surface is considered definitely "smooth" (*e.g*. generating a low backscatter response) if :

$$h < \lambda / (25 \cos \theta) \qquad (2)$$

(Ford, 1998).

Assuming the AIRSAR/TOPSAR system parameters for these data sets, the following rms height definitions for "rough" and "smooth" surface roughness were calculated using Eq (1) and Eq. (2) for the minimum and maximum look angles across the radar acquisition swath. No allowance is made for topographic relief and the incident angle, $\theta_i$, is assumed to be equivalent to $\theta_{loc}$ and the survey look angle (Figures 7a&b).

Table 1 highlights the potential variation of the AIRSAR/TOPSAR response to look angle across the swath of the imagery (Figure 2) without taking the topographic effects into account. P, and to a lesser extent L radar band, are more likely to observe a "smooth" radar surface at the far swath extent or range of the imagery while C band is most likely to register rough radar surfaces at the near swath range (Table 1). The P band radar imagery is also most likely to discriminate the roughest surface nature at the nearest swath extent of the imagery. The question of whether the surface is a thick vegetation canopy or rocky ground surface is also affected on the ability of the longer wavelength radar to penetrate vegetation and also its signature polarisation. As discussed in Section 1.1 and illustrated in Figure 3, volume scattering measured by P band (and to a lesser extent L band) with a HV polarisation provides the optimal imagery to observe geologically related surface roughness beneath vegetation canopy. HV is also optimal for minimising the effects of variable local incident and look angles (Tapley, 2002).

| **AIRSAR/TOPSAR Band** | **C** | **L** | **P** |
|---|---|---|---|
| **Wavelength (λ, cm)** | **5.7** | **25** | **68** |
| ***Response at far swath range :*** | | | |
| "Rough" rms height (cm) @ $\theta_i$ = 68 degrees | >3.5 | >15.2 | >41.3 |
| "Smooth" rms height (cm) @ $\theta_i$ = 68 degrees | <0.6 | <2.7 | <7.3 |
| ***Response at near swath range :*** | | | |
| "Rough" rms height (cm) @ $\theta_i$ = 25 degrees | >1.4 | >6.3 | >17.1 |
| "Smooth" rms height (cm) @ $\theta_i$ = 25 degrees | <0.3 | <1.1 | <3.0 |

Table 1 Definitions of smooth and rough radar surfaces for AIRSAR/TOPSAR radar band wavelengths and maximum-minimum range of look angles where Look angle = Incident angle, assuming a flat ground surface.

Studies by Huadong *et al*., (1996) using shuttleborne C and L band multi-polarisation radar found that L band HV polarised imagery was the best combination for discriminating two different basalt units, alluvium and bedrock. Kierein-Young *et al*. (1992) showed that quantifiable estimates of surface roughness rms is possible in an arid environment such as Death Valley, Nevada. Height rms values were calculated from modelling the fractal dimensions of the C, L and P band power spectral density however the model assumed generally smooth playa to partly smooth alluvial surfaces (Kierein-Young *et al*., 1992). Subsequent communication with one of the authors, indicated that in thickly forested environments there are wavelength-specific problems related to partial canopy penetration, leaf moisture dielectric effects and canopy/understory vegetation cover that combine to make this a difficult problem (Kruse, pers. comm.). The observation of surface roughness is also identified by Raney (1998) to be more subtle and less quantifiable with increasing penetration through vegetation cover. Ford (1998) also notes that estimation of surface roughness using multi wavelength radar can be possible within sparsely vegetated terrains.

### 2.2.3 Dielectric properties and Moisture

Another factor that can effects radar backscatter is the dielectric property and related moisture content of the surface materials. Such dielectic properties influence the attenuation and reflectance of the electric field component of the radar pulse. Most rocks exhibit a narrow range in dielectric properties however they will vary significantly as a function of water moisture, its porosity and water holding capacity (Ford, 1998). Water can strongly limit the ground penetration of even the longer wavelength L and P band radar when interacting with moist soil and regolith (Ford, 1998) (Figure 8). As a consequence the radar backscatter response can vary between geological units when they contain different weathered regolith profiles affecting their porosity and moisture content.

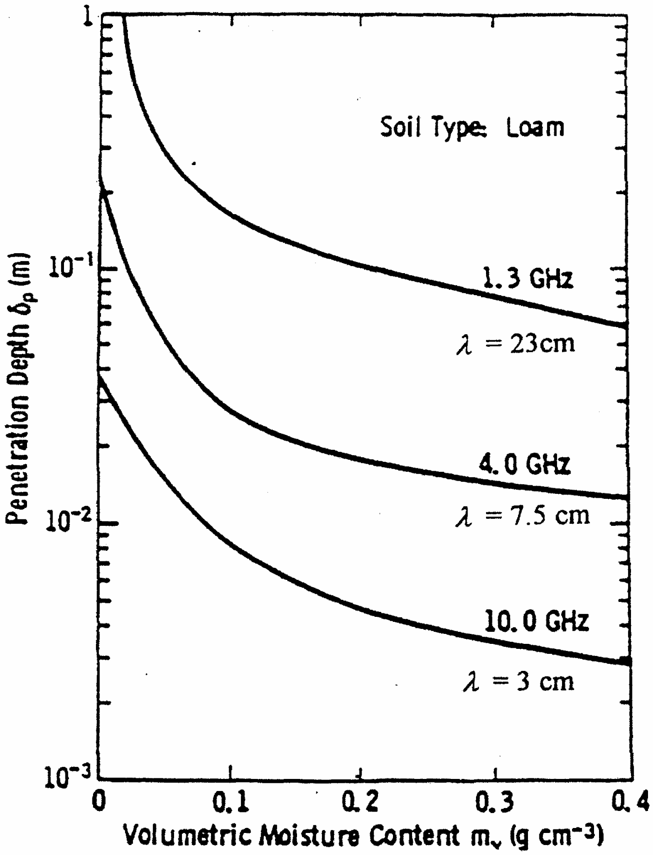


Figure 8 Penetration depths for soil with different moisture contents at different wavelengths *e.g.* C band (λ ~ 3cm) and L band (λ ~ 23cm), after Dobson (1993).

### 2.3.4 Combined QC issues

The effect of the variable incident angles across each individual flight swaths upon the returned backscatter limits the ability to simply mosaic radar imagery, particularly if flights are in opposite look angle directions (*e.g.* TS1339 acquired with NE range versus the SW range acquired TS1340 and TS1297). Consequently the presence of radar shadowing and layover will change according to the topographic relief (Section 2.3.1). Such variable look and hence incident angles will also significantly affect the response of surface roughness across the swath for each AIRSAR wavelength (Section 2.3.2). Changes in vegetation and/or soil moisture due to precipitation between flights could also affect radar backscatter however the acquisition of all three flights on 17/8/2000 makes this a more unlikely influence of image boundary differences. Due to the complexity of these various effects, no attempt has been made to level the radar products.

# 3 Results

## 3.1 TOPSAR DEM

### 3.1.1 Image products

The TOPSAR DEM product processed from the three Tasmanian flight lines appeared to generate good quality data at 5 metre spatial sampling that mosaicked well as a combined DEM data set encompassing 1440 $km^2$ and a range of elevation between 3 to 1370 metres. Examples of the mosaicked DEM product as an image, as a shaded relief (illuminated at 45 degree NE and 60 elevation) and a topographic modelled slope, are shown in Figures 9a, 9b and 9c respectively.

Associated with the supplied TOPSAR DEM product are imagery representing estimates of the local incidence angle (0-180 degrees) to assist in the interpretation of the radar acquisition. Each acquisition will generate a specific incidence angle product relevant for the flight line track and look direction. Figure 10 shows the example of the incidence angle estimates for flight line, TS1340. The lower incident angles shown along the north eastern areas of the imagery generally correspond to the lower radar look angles operating by the AIRSAR/TOPSAR as it flew along a flight path just beyond the NE of the imagery (Figure 10). Although the range of look angle available by the survey is restricted by the system specification, the effective incidence angle will be dependent according to the local incident angle as shown in Figure 7b. As discussed previously, such areas dominated by lower incident angles will be more susceptible to layover distortion while radar shadow effects will increase at the higher incident angles (Figure 10).

A statistical comparison between the overlapping DEM results for the TOPSAR acquisitions (Figure 11) was undertaken to evaluate the consistency of the derived elevations and registration procedure (Appendix 2). Although there appeared spurious variations for the minimum and maximum elevations values, the correlation coefficients were greater than 0.99, and the median / mean values showed a less than 5 metres difference (Appendix 2).

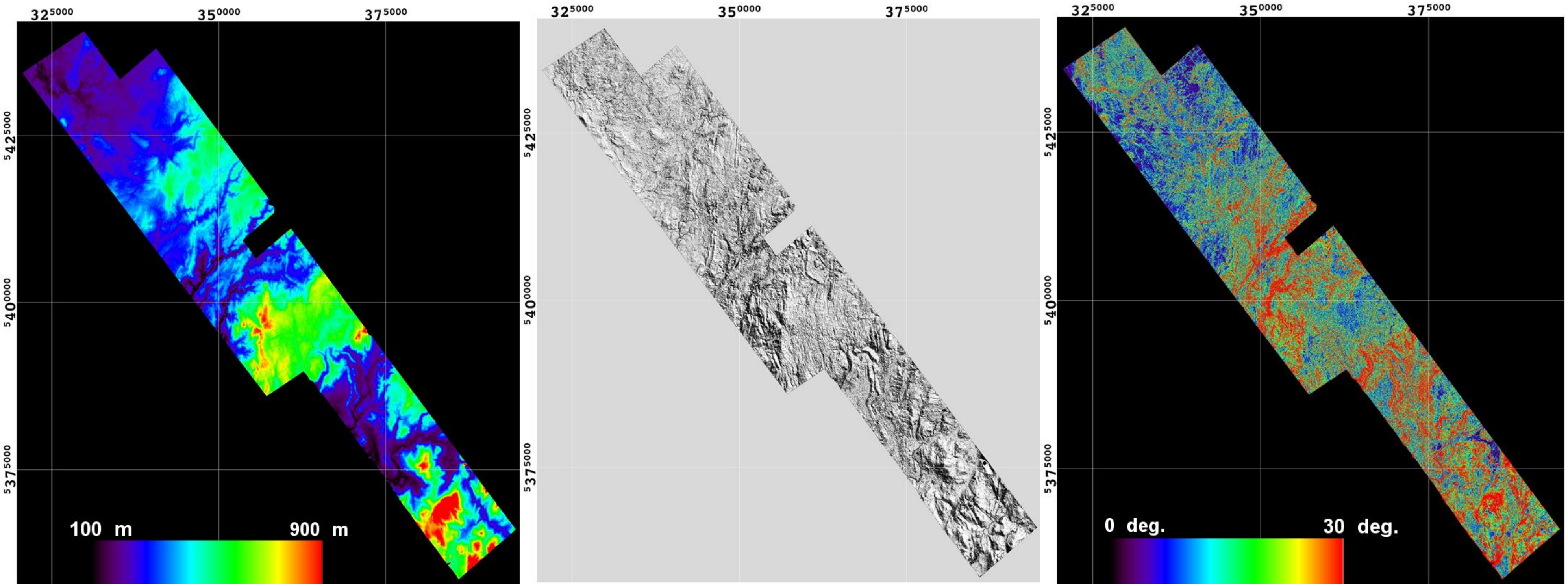


a) b) c)

Figure 9 a) TOPSAR DEM mosaic of TS1297, TS1339 and TS1340 acquisitions displayed with a linear 100 to 900 metre elevation stretch; b) Shaded mosaic illuminated with 45$^{o}$ NE azimuth and 60$^{o}$ elevation; and c) Slope mosaic product displayed with a linear 0 to 30 degrees slope stretch. All imagery is registered for GDA94 MGA Zone 55

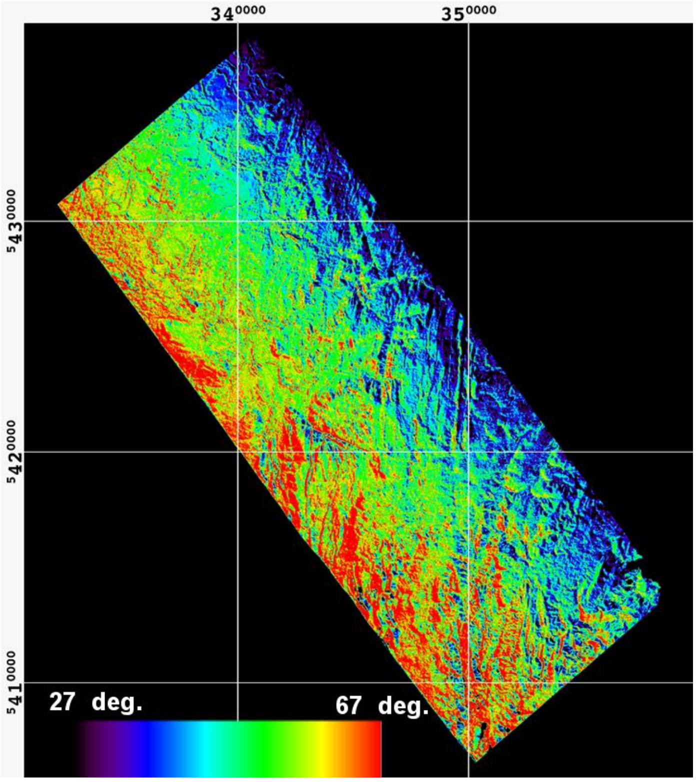


Figure 10 Supplied calculated local incident angle estimates for flight line TS1340.

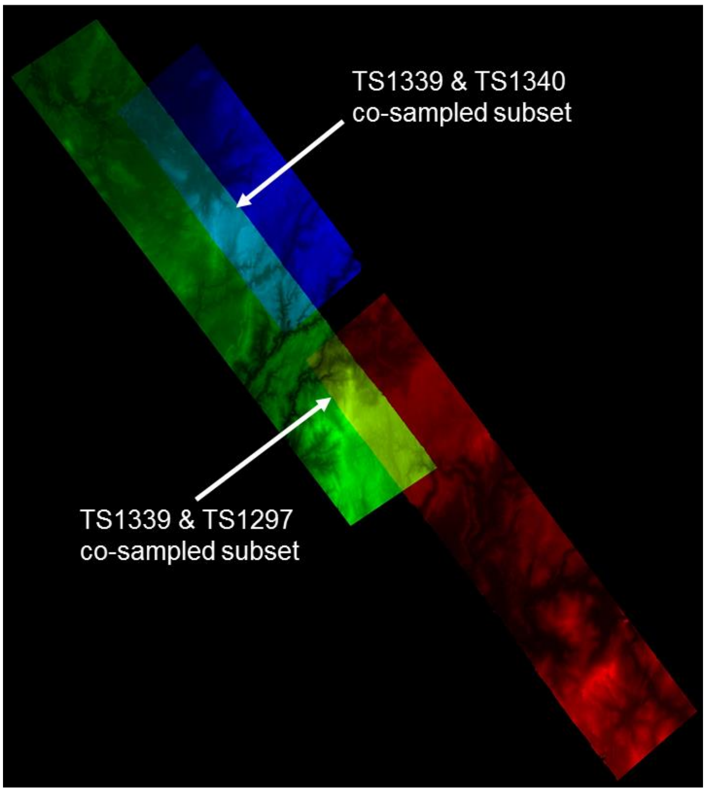


Figure 11 Depiction of the three TOPSAR acquisitions and their overlapping areas. The spatial extent is the same as shown in Figure 9 a-c).

### 3.1.2 Comparison with SRTM 25m, Photogrammetric derived and LiDar DEMs

Statistical comparisons between the mosaicked TOPSAR DEM product and the MRT supplied SRTM 25 metre, photogrammetric derived and LiDar DEMs was undertaken to assess its quality. Issues of variable spatial sampling resolution and registration between these four datasets is potentially relevant however it was still seen as a useful exercise for validation. ERDAS ERMapper™ software was used to calculate the statistics and subset according to their spatial extents. Table 2 shows the comparison between the TOPSAR SRTM 25 metre, photogrammetric derived DEMs, while Table 3 shows the comparison for the significantly smaller coincident area encompassing all four DEMs including SRTM 25 metre, photogrammetric and LiDar derived DEMs. The relevant LiDar data sets for this comparison were the Meredith, South1 and North1 acquisitions. The statistics for the two coincident areas showed that although the TOPSAR DEM exhibited significantly lower minimum values than the other DEMs, the overall comparison was favourable with a correlation of 0.996 and higher (Table 2 and 3).

| | **TOPSAR** | **SRTM 25m** | **Photogrammetry** |
|---|---|---|---|
| **Area (Hectares)** | 144029 | 144029 | 144029 |
| **Spatial sampling (m)** | 5 | 25 | 25 |
| **Minimum** | 3.1 | 54.6 | 50.0 |
| **Maximum** | 1369.8 | 1246.8 | 1266.6 |
| **Mean** | 365.1 | 364.2 | 361.4 |
| **Median** | 334.1 | 329.4 | 325.6 |
| **Std.Dev.** | 163.4 | 164.0 | 165.9 |
| | | | |
| **CorrelationMatrix** | **TOPSAR** | **SRTM 25m** | **Photogrammetry** |
| **TOPSAR** | 1 | 0.997 | 0.996 |
| **SRTM25m** | 0.997 | 1 | 0.999 |
| **Photogrammetry** | 0.996 | 0.999 | 1 |

Table 2 Statistical comparison between coincident TOPSAR, SRTM 25m and Photogrammetry derived DEMs.

| | TOPSAR | SRTM 25m | Photogrammetry | LiDAR |
|---|---|---|---|---|
| **Area (Hectares)** | 17653 | 17653 | 17653 | 17653 |
| **Spatial sampling (m)** | 5 | 25 | 25 | 0.5 - 2.0 |
| **Minimum** | 3.5 | 102.6 | 97.0 | 95.0 |
| **Maximum** | 917.0 | 915.8 | 920.0 | 1160.6 |
| **Mean** | 434.5 | 437.1 | 434.7 | 434.0 |
| **Median** | 481.7 | 483.8 | 479.6 | 478.0 |
| **Std.Dev.** | 166.3 | 162.9 | 164.8 | 164.3 |
| | | | | |
| **CorrelationMatrix** | **TOPSAR** | **SRTM 25m** | **Photogrammetry** | **LiDAR** |
| **TOPSAR** | 1 | 0.998 | 0.998 | 0.996 |
| **SRTM25m** | 0.998 | 1 | 0.999 | 0.998 |
| **Photogrammetry** | 0.998 | 0.999 | 1 | 0.998 |
| **LiDAR** | 0.996 | 0.998 | 0.998 | 1 |

Table 3 Statistical comparison between coincident TOPSAR, SRTM 25m, Photogrammetry and LiDar derived DEMs.

A further analysis was undertaken to assess the accuracy of the elevations and spatial Easting and Northing coordinates of the TOPSAR, relative to the other supplied DEMs and, in particular, to the 1:25,000 topographic mapping. The effect of the geology on the derived DEM elevation values was also briefly examined. In particular, two statistical training subsets were chosen from the areas with coincident DEM coverage, one encompassing the Meredith intrusives (Dg, Dga), and another with no Meredith intrusives, dominanted by the Mt Read volcanics (Figure 12). The statistical results for each of the two training areas and the entire coincident DEM area are listed in Appendix 3. There again appeared differences between the minimum and maximum DEM values from spurious outliers however the mean and median values were fairly similar within both the Meredith and non Meredith granitic areas. The Meredith Granite area showed a smaller variation in median elevations than the volcanic terrain (*e.g*. 3.82 m cf 7.06 m) (Appendix 3). The correlation coefficients were generally high for both areas although the volcanic terrain showed higher values (> 0.998) compared to the Meredith granite (> 0.95). However a spurious LiDar maximum of 1160 metres possibly generated this difference.

A detailed comparison between the DEM data sets was also undertaken using five spot topographic peaks within both training areas (Table 4). The supplied 1:25,000 topographic mapping with surveyed elevations were used as a reference to calculate the difference ("**Δ(1:25,000)**") relative to the four DEM data sets (Table 4). No significant differences were observed and generally within 50 metres coordinate accuracy and better than 15 metres elevation accuracy. There was potentially subjectivity in choosing the position of the topographic peaks from the various DEMs which may explain the discrepancy of the Mt Sale Lidar result (Table 4). These results appeared consistent with estimates of spatial x-y registration errors suggested by the Root Mean Square (rms) values obtained for the first order polynomial transformation for each individual TOPSAR flight line (Appendix 1). In particular, rms values ranged from between 4.5 and 9.4 pixels (*e.g.* 24 to 47 metres) (Appendix 1).

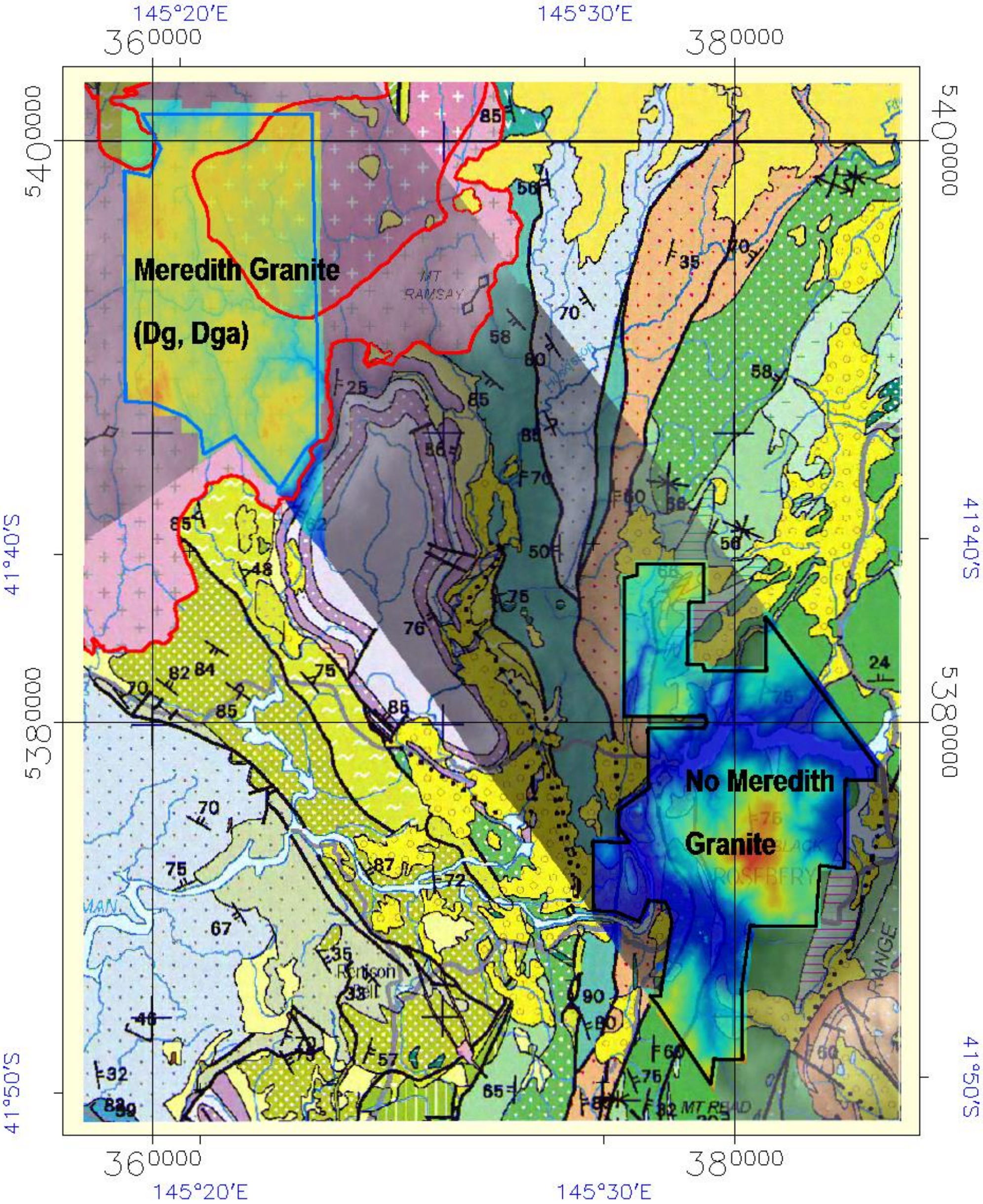


Figure 12 Areas of coincident TOPSAR (blue:low; red:high), SRTM 25m, Photogrammetric 25m and LiDar DEMs overlaying 1:250,000 geology. The Meredith Granite (DG, Dga – red boundary, blue subset) and non-Meredith granite (black subset) highlight the two training areas for statistical comparison. The mosaicked TOPSAR DEM survey area is shown in grey.

| Coordinates (GDA94) | Mt Black | Δ(1:25,000) | Mt Sale | Δ(1:25,000) | Burns Peak | Δ(1:25,000) | | Δ(1:25,000) | | Δ(1:25,000) |
|---|---|---|---|---|---|---|---|---|---|---|
| **1:250,000 Geology:** | **Ɛdv** | | **Ɛdv** | | **Ɛdsvl** | | **Dg/Dga** | | **Dg/Dga** | |
| (Easting) 1:25,000 | 380647 | | 382944 | | 378385 | | 363972 | | 362842 | |
| (Northing) 1:25,000 | 5375580 | | 5377974 | | 5384652 | | 5394495 | | 5398980 | |
| (Elev.) 1:25,000 | 929 | | 521 | | 660 | | 584 | | 623 | |
| (Easting) TOPSAR | 380642 | -5 | 382932 | -12 | 378373 | -12 | 363963 | -9 | 362839 | -3 |
| (Northing) TOPSAR | 5375598 | 18 | 5377978 | 4 | 5384656 | 4 | 5394546 | 51 | 5399011 | 31 |
| (Elev.) TOPSAR | 916 | -13 | 532 | 11 | 652 | -8 | 588 | 4 | 621 | -2 |
| (Easting) SRTM25m | 380667 | 20 | 382895 | -49 | 378395 | 10 | 363995 | 23 | 362867 | 25 |
| (Northing) SRTM25m | 5375604 | 24 | 5377940 | -34 | 5384678 | 26 | 5394451 | -44 | 5398991 | 11 |
| (Elev.) SRTM25m | 916 | -13 | 525 | 4 | 653 | -7 | 572 | -12 | 612 | -11 |
| (Easting) Photogram. | 380626 | -21 | 382923 | -21 | 378363 | -22 | 363977 | 5 | 362839 | -3 |
| (Northing) Photogram. | 5375611 | 31 | 5377980 | 6 | 5384652 | 0 | 5394498 | 3 | 5398991 | 11 |
| (Elev.) Photogram. | 920 | -9 | 520 | -1 | 650 | -10 | 580 | -4 | 620 | -3 |
| (Easting) LiDAR | 380644 | -3 | 382848 | -96 | 378401 | 16 | 363991 | 19 | 362857 | 15 |
| (Northing) LiDAR | 5375591 | 11 | 5377960 | -14 | 5384637 | -15 | 5394510 | 15 | 5398970 | -10 |
| (Elev.) LiDAR | 927 | -2 | 528 | 7 | 662 | 2 | 582 | -2 | 621 | -2 |

Ɛdv : Felsic to intermediate calc-alkaline volcanic rocks, (Central Volcanic Complex and correlates / Mt Read Volcanics)

Ɛdsvl : Felsic lava within Western Volcano-Sedimentary Sequence and correlates
Dg/Dga : Meredith granite and associated intrusives

Table 4 Spot comparisons between the TOPSAR, SRTM25m, Photogrammetric 25m and Lidar DEMs with five 1:25,000 topographic located hilltops.

## 3.2 TOPSAR multi-wavelength and multi-polarimetric products

The image products from the three AIRSAR/TOPSAR acquisitions were imported into an ERDAS ERMapper$^{TM}$ algorithm style GIS database incorporating ancillary MRT supplied vector and raster files of other DEMs, SPOT imagery, orthophotography, geology, vegetation, and airborne geophysics. Two areas within TS1340 were studied in particular in order to observe the effects of incident angle, wavelength and polarisation as well as compare with published geological and vegetation information (Figure 13). In particular it was attempted to examine the issues of the potentially competing backscattering effects of vegetation versus geological. Figure 13 also shows the enhanced backscatter of the C band VV polarisation (Cvv) near swath range along the north eastern edge of the image associated with the lower incident angle.

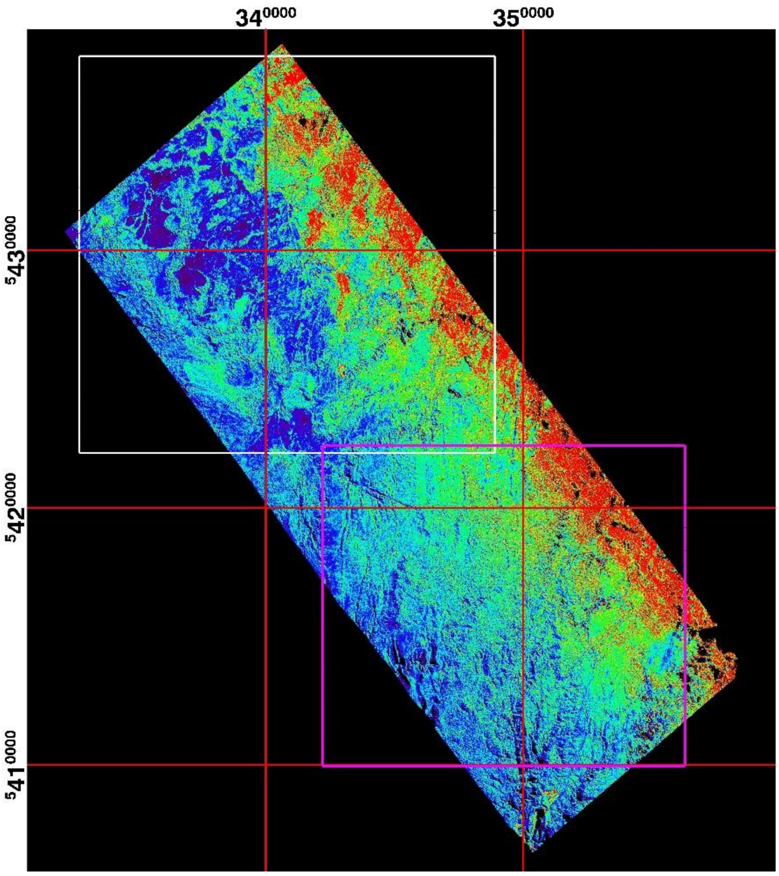


Figure 13 AIRSAR/TOPSAR Cvv image of flight line TS1340 showing the locations of the vegetation (white box) and geological (magenta box) study areas.

### 3.2.1 TS1340 Northern study area

The northern portion of flight line TS1340 proved an useful area for examining the response of the multi -wavelength and -polarisation radar to discriminate vegetation where limited geological outcrop and diversity of units appeared apparent by the published 1:250000 geology (Figure 14a). A range of temperate rainforest and vegetation occupies this area from the steep hills and gullies to swampy floodplains (Figure 14b). Figure 14c highlights this topography and limited geological units mapped within this lowland dominated terrain. The predominant mapped unit is the Cowrie Siltstone intruded by with mostly narrow north-easterly trending Tayatea Dyke Swarm dolerite bodies. There is a significant variation in vegetation from swampy moorland grasses to wet rainforest to open woodland (Figure 14d). Figure 14d also indicates the short wavelength and vertically polarised Cvv band exhibits an exaggerated bias in backscatter related to lower incident angles (*e.g.* compare with Figure 10).

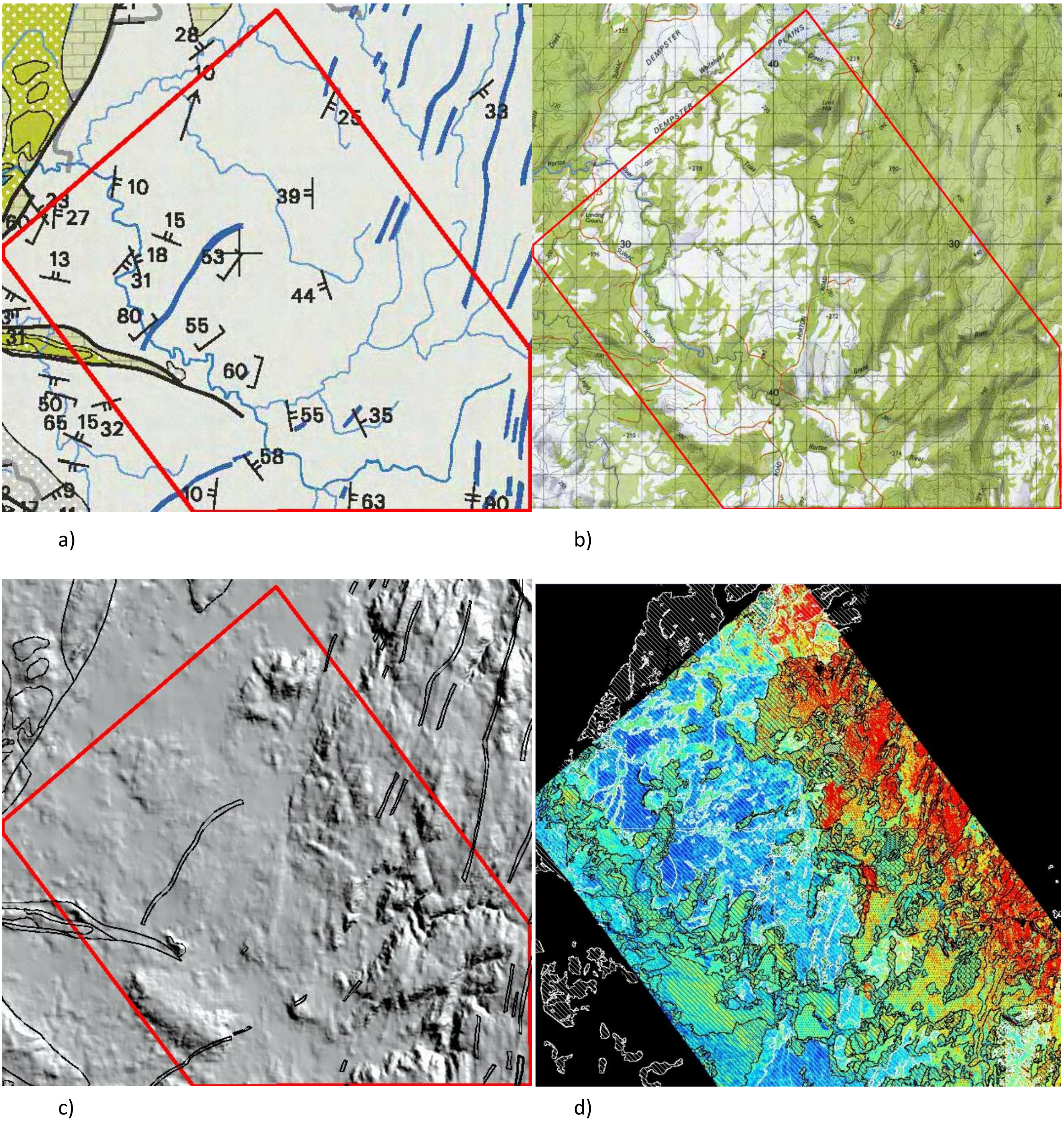


Figure 14 a) Published 1:250000 geology of the vegetation study area; b) 1:100000 topographic map; c) shaded SRTM 25m DEM with 1:250000 geology overlay; d) Pseudo coloured Cvv backscatter response (blue:low backscatter return; red high backscatter) with 1:25,000 vegetation overlay. Black hatch: Eucalyptus obliqua wet forest (WOU), white hatch : Buttongrass moorland (MBU); black stipple : Nothofagus-Phyllocladus short rainforest (rms); black cross hatch : Eucalyptus nitida dry forest and woodland (DNI).

The Lhv band and polarisation (Figure 15) and Phv, showed a better comparison between the 1:25000 vegetation classification than the Cvv band (Figure 14d). There appeared less lower incident angle bias with this longer wavelength cross polarised bands, producing similar backscatter responses for the same vegetation class throughout the imagery. For example the Buttongrass moorland is indicated by a consistently low backscatter return (Figure 15).

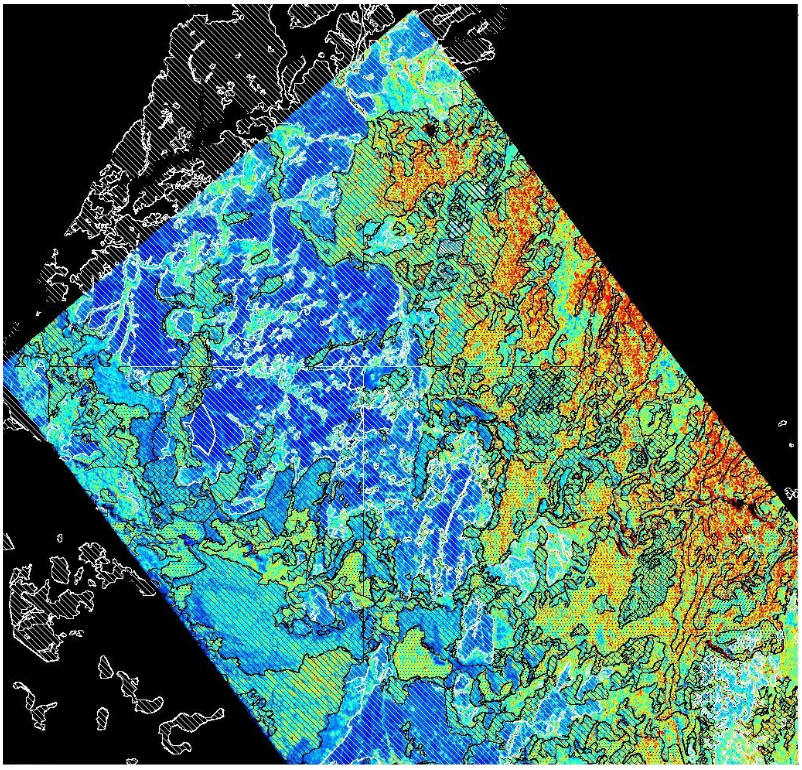

Figure 15 Pseudo coloured Lhv backscatter response (blue:low backscatter return; red high backscatter) with 1:25000 vegetation overlay. Black hatch: Eucalyptus obliqua wet forest (WOU), white hatch : Buttongrass moorland (MBU); black stipple : Nothofagus-Phyllocladus short rainforest (rms); black cross hatch : Eucalyptus nitida dry forest and woodland (DNI).

A closer comparison of the higher resolution TOPSAR DEM with SRTM 25m DEM and the published geology reveals that subtle extensions to the north easterly trending Tayatea Dyke Swarm dolerite bodies (Figure 16). The improvement in spatial resolution from the 25 metre SRTM (Figure 14c) to the 5 metre airborne TOPSAR (Figure 16) appears to significantly enhance the potential geological interpretation.

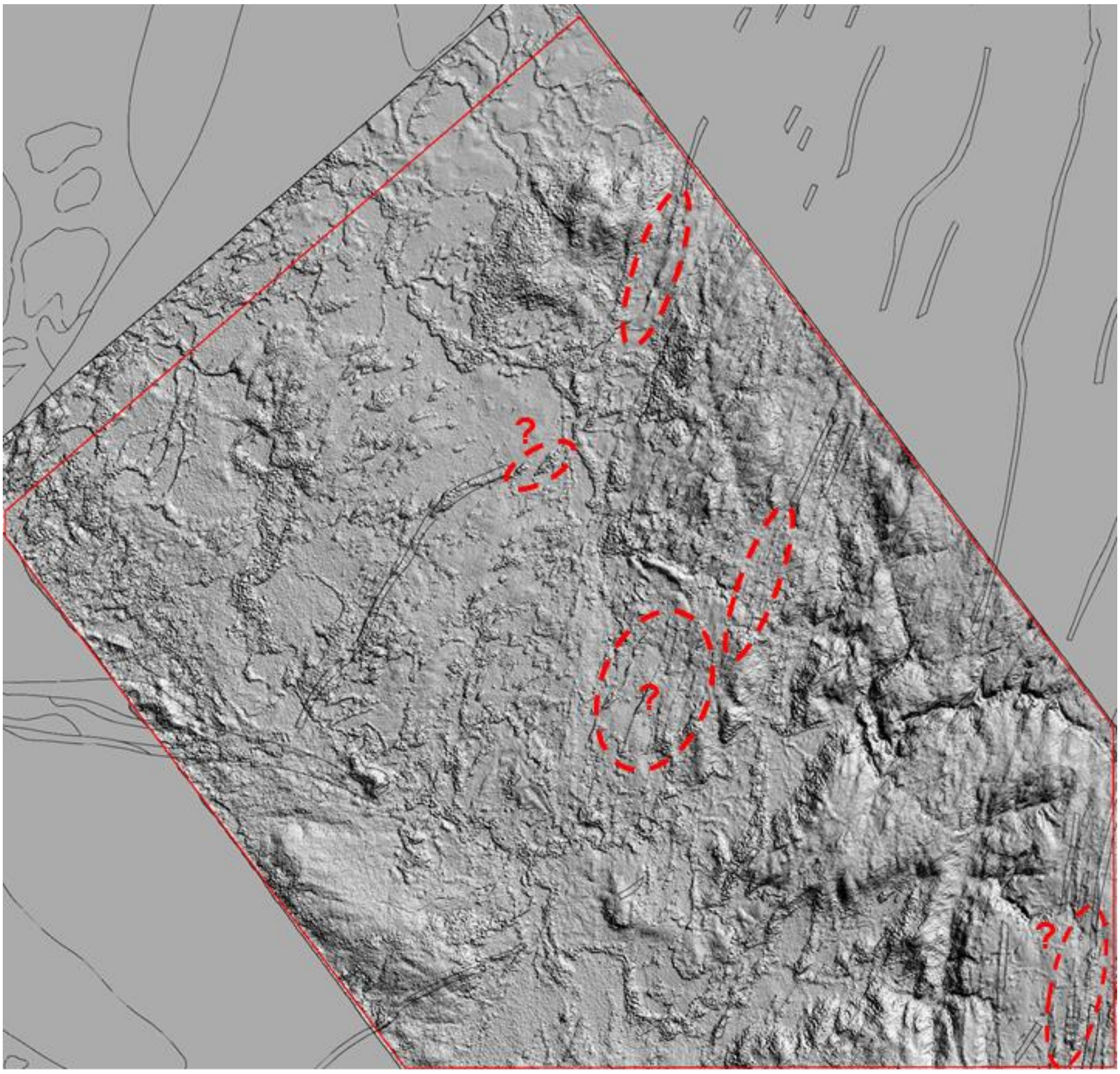

Figure 16 Artificially shaded TOPSAR DEM (45 deg. NE azimuth, 60 deg. elevation) with 1:250000 published geology. Suggested extensions or presence of dolerite dykes are highlighted within dashed red ellipses.

### 3.2.2 TS1340 Southern study area

The 1:25,0000 topographic mapping of the southern TS1340 area shows a more deeply incised relief with several watercourses including the Donaldson River (Figure 17a). The published 1:25,0000 geology indicates a mixture of Cowrie Siltstone, metasedimentary units, and dolerite dyke intrusives overlain by Tertiary basalts (yellow) (Figure 17b). The radiometrics imagery appears only useful for highlighting the Cowrie Siltstone and Balfour Subgroup (Figure 17c) while the aeromagnetics shows the importance of the north and northeast trending structures and boundaries (Figure 17d).

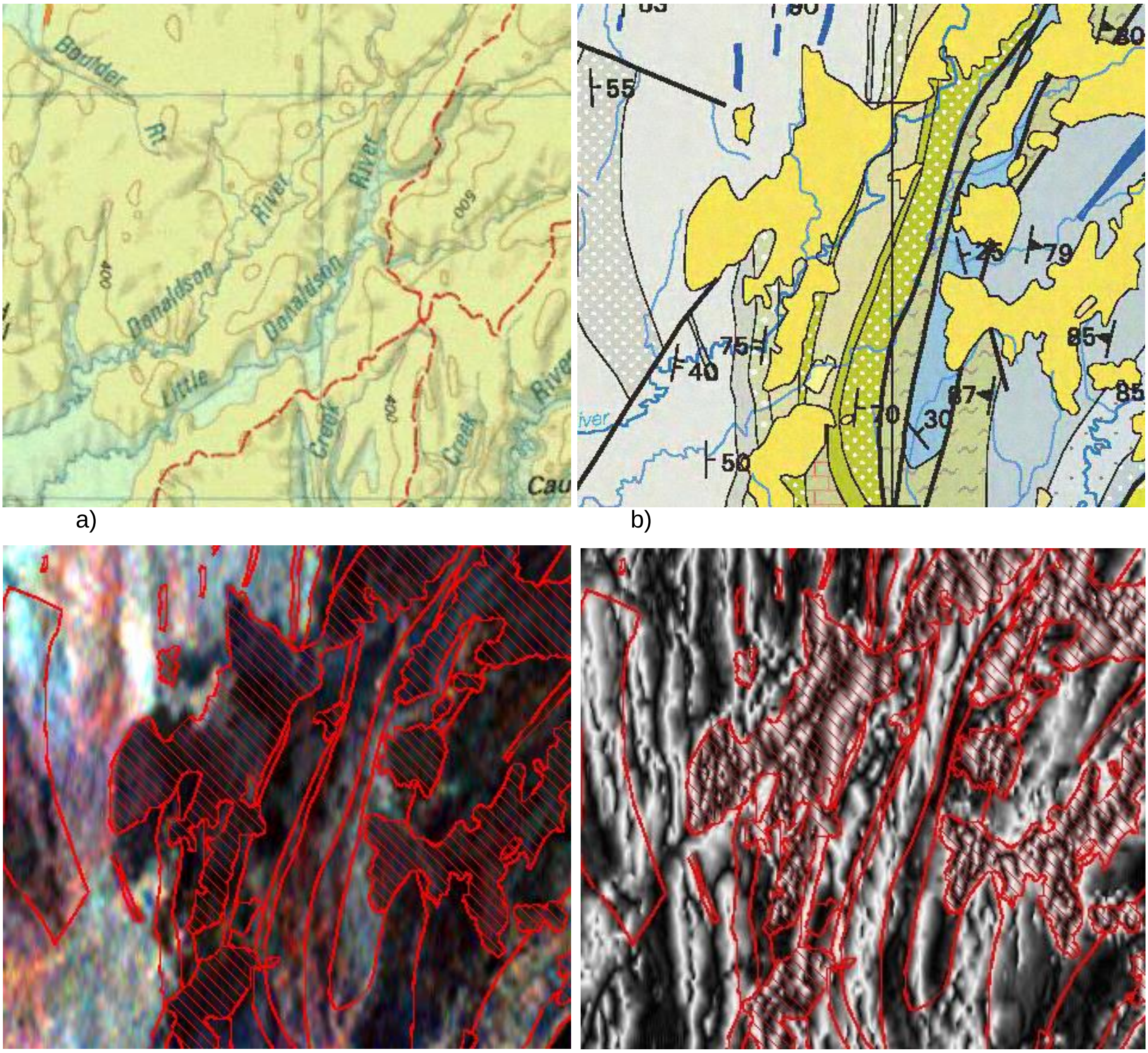


a) b)

c) d)

Figure 17 a) 1:25,0000 topographic map of TS1340 southern study area as shown in Figure 13; b) 1:2500000 published geology with Tertiary basalt highlighted in yellow; c) Radiometric Ternary image (RGB : KThU) with geology overlay. Tertiary basalt highlighted within red hatched area; d) High frequency Tilt filtered aeromagnetics. Tertiary basalt highlighted within red hatched area.

The TOPSAR DEM product (Figure 18b) again shows a significant improvement over the SRTM 25 DEM (Figure 18a). Subtle north trending elevation features appear to be associated with dolerite dykes and their possible extension (Figure 18b).

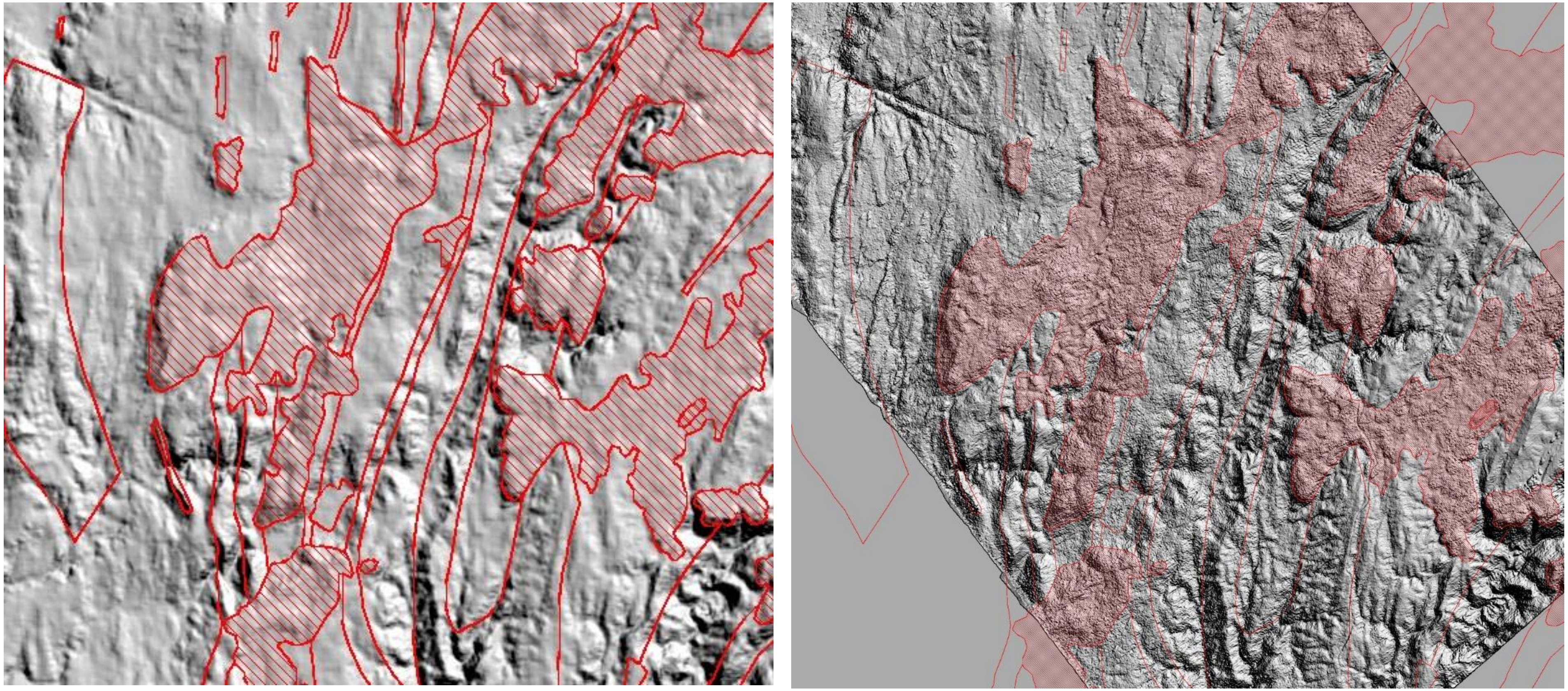

Figure 18 a)  Shaded SRTM 25m DEM (45 deg. NE azimuth, 60 deg. elevation) with 1:25,0000 geology overlay. Tertiary basalt highlighted within red hatched area. b) Shaded TOPSAR DEM (45 deg. NE azimuth, 60 deg. elevation) with 1:25,0000 published geology overlay. Tertiary basalt highlighted within red hatched area.

An examination of the various multi-wavelength and -polarimetric bands with the published geology indicated that optimal results were obtained with Phv imagery (Figure 19). A north westerly fault line transecting the Balfour Subgroup sedimentary units (“A”) was clear within the DEMs and the Phv imagery (Figure 19). There also appeared to be a Phv anomalous area encompassing and larger than the presently mapped dolerite Tayatea Dyke nearby (“B”) although this response wasn’t replicated elsewhere (Figure 19). The overlying Tertiary basalt shows a consistently moderate to high Phv backscatter within areas shown by hatching (“C”) (Figure 19). The Arthur Metamorphic Complex unit appears to have the highest surface roughness related backscatter (“D”) while the Cowrie Siltstone shows a generally low backscatter  (“E”) (Figure 19). The same area also has a diversity of vegetation types (Figure 20). Anomalous areas, “B” and “D” shown in Figure 19, also appear to have classified vegetation boundaries associated with them (Figure 20). It is possible that geobotanical associations coexist with these geological units. Further ground truthing which assist an understanding of such geological-vegetation spatial relationships.

RGB colour composite imagery combining the various bands and polarisations did not generally produce imagery that clearly discriminated either vegetation or geology. A RGB image consisting of Phh, Pvv and Phv showed some subtle variations in hue across the various units (Figure 21). The greatest benefit appeared to be the highlighting of topographic features, possibly related to geological structure or lineaments (Figure 21).

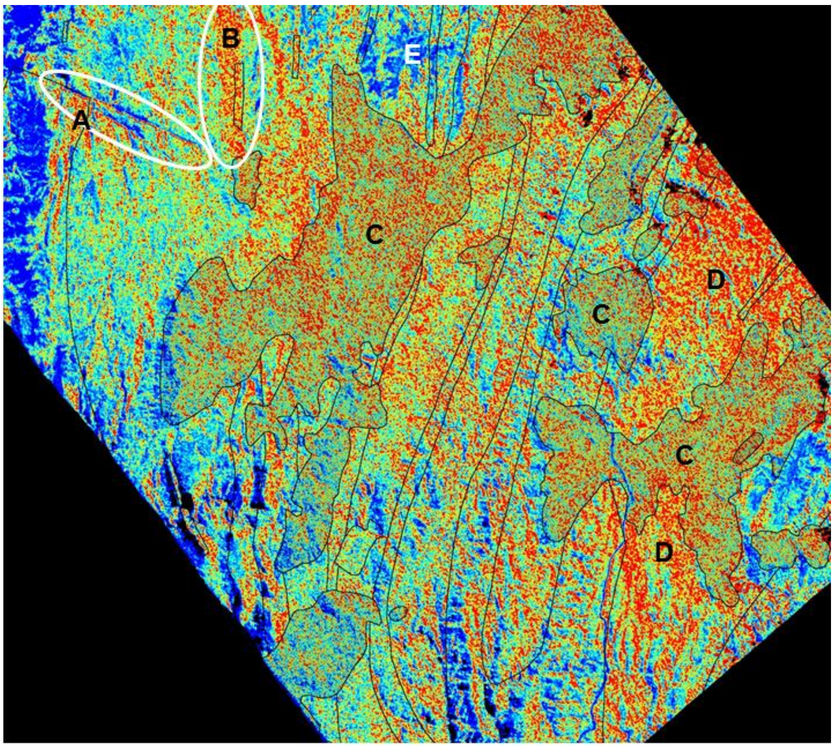


Figure 19 Pseudo coloured Phv backscatter response (blue:low backscatter return; red high backscatter) with 1:250000 geology overlay. Tertiary basalt highlighted within hatched area.

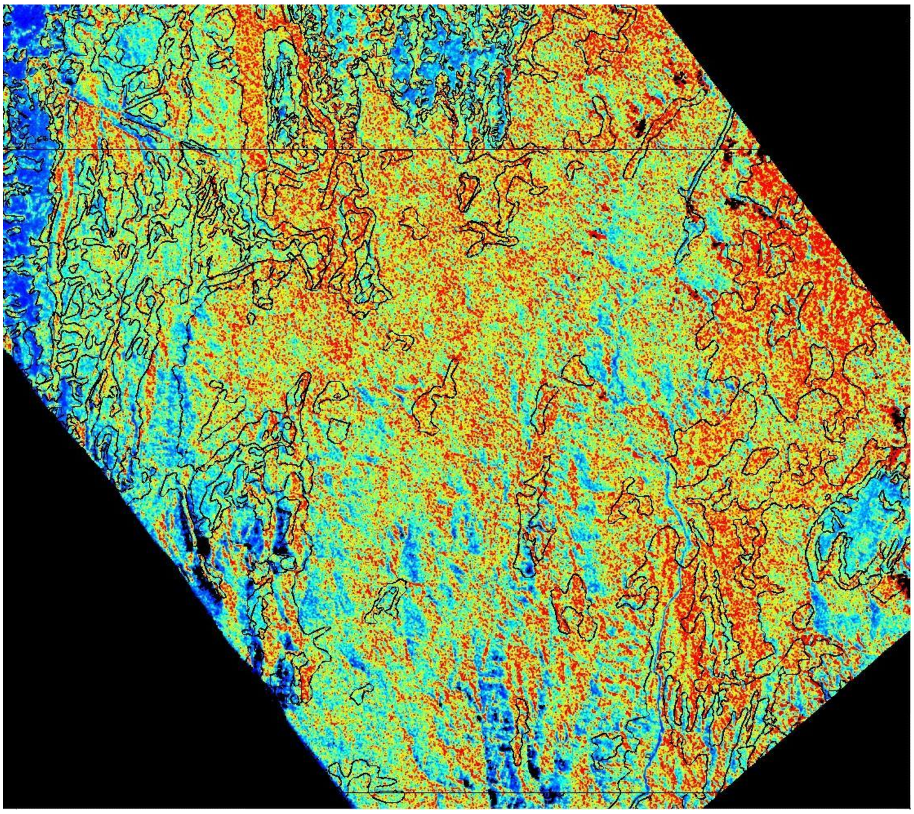

Figure 20 Pseudo coloured Phv backscatter response (blue:low backscatter return; red high backscatter) with 1:25,000 vegetation overlay.

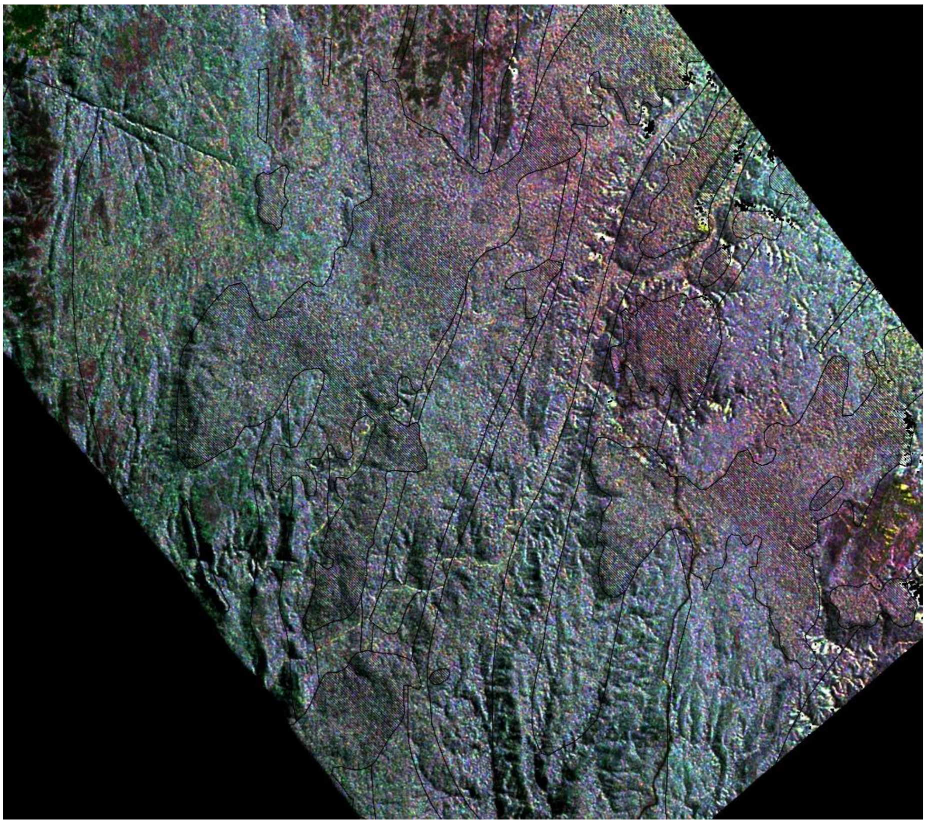

Figure 21 RGB composite image of Phh, Pvv, Phv backscatter response with 1:25,0000 geology overlay.

### 3.2.3 Mosaicked polarimetric imagery

Mosaicked results combining the three flight lines of multi-wavelength and -polarimetric data were affected by the issues described in Section 2.3.4. RGB colour composite products for the combined Cvv, Ltp and Ptp products showed that a uniform linear stretch for the three acquisitions produced such boundary issues (Figure 22a). However the application of independently calculated 99 percent linear stretching for each acquisition generally improved the mosaicked product (Figure 22b). This effect was most notable for bands such as the Cvv (Figure 23a). An improvement in mosaicked results were generated using Phv and gave similar results whether an uniform or independent flight line linear stretching was applied (Figure 23b). This is consistent with the description earlier that the cross-polarized HV scattering bands are less dependent on incidence angle (and therefore, terrain), than the co-polarized (HH and VV) backscatter (Tapley, 2002).

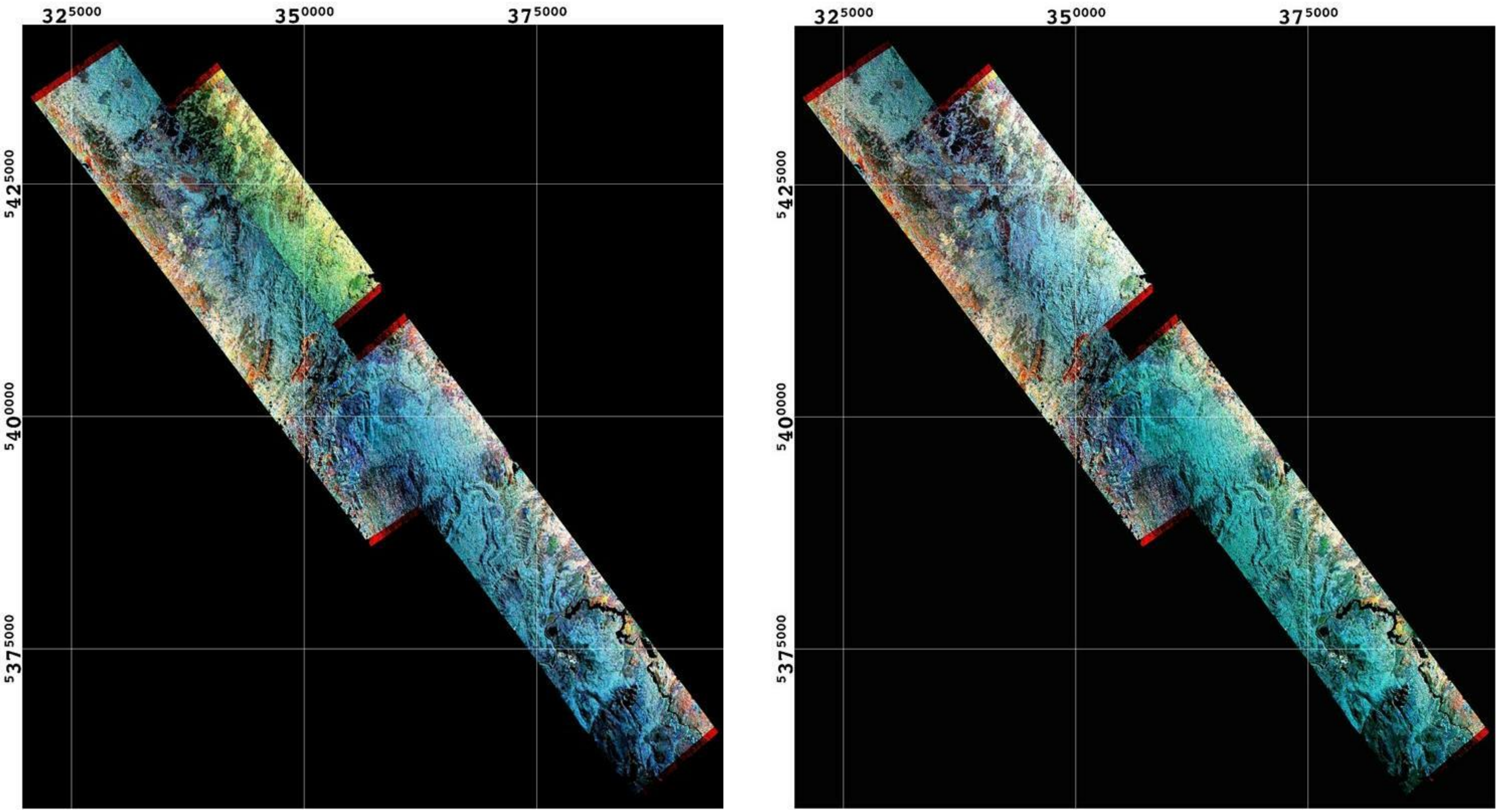


a) b)

Figure 22 a) RGB composite of Cvv, Ltp and Ptp with uniform linear stretch applied to each band of combined TOPSAR acquisitions; b) RGB composite of Cvv, Ltp and Ptp with 99.0% linear stretch applied independently to each band of TS1297, TS1339 and TS1340. All imagery is registered to GDA94 MGA Zone 55.

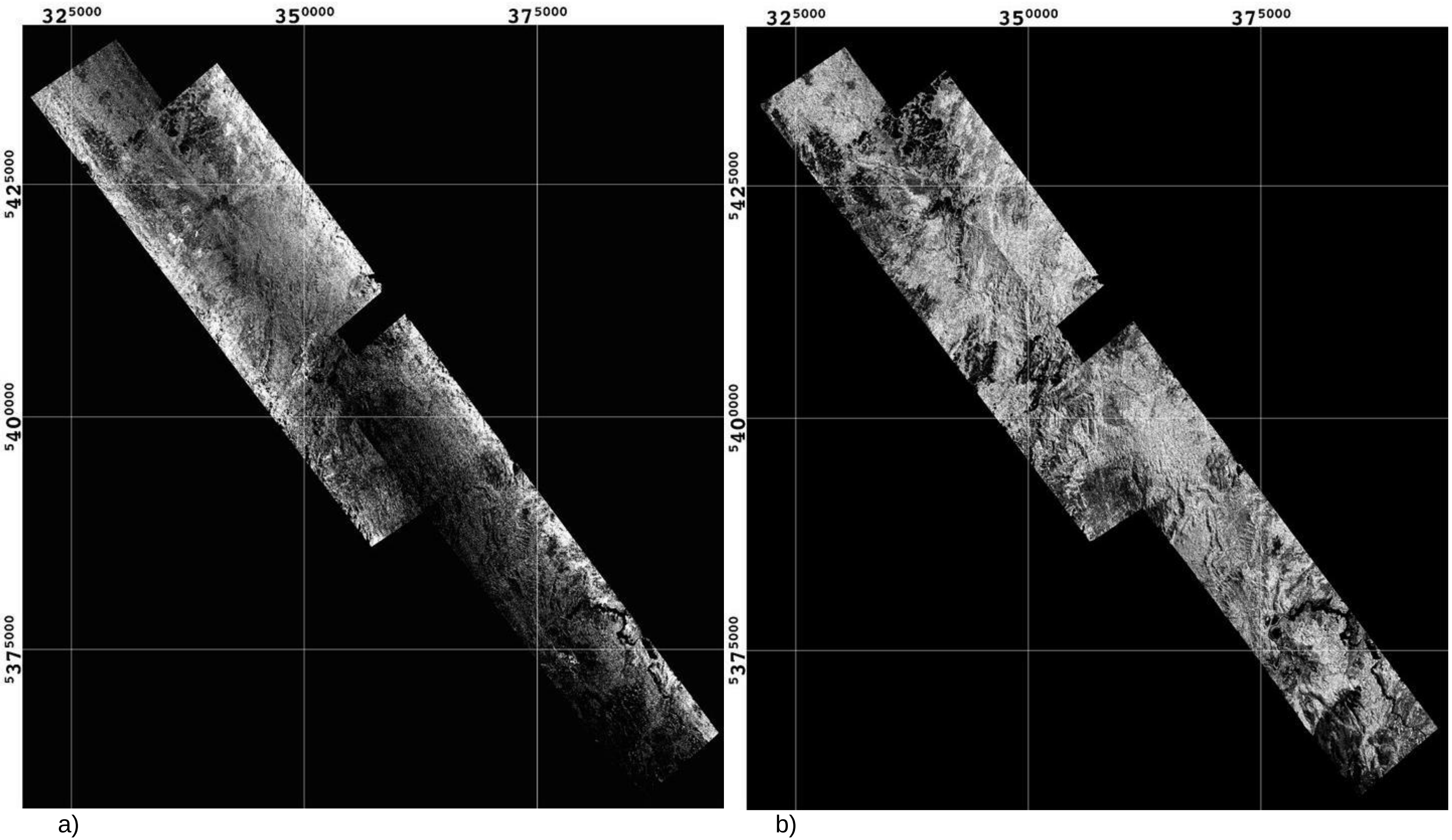


Figure 23 a) Greyscale imagery of Cvv with 99.0% linear stretch applied independently to each band of TS1297, TS1339 and TS1340; b) Greyscale imagery of Phv with uniform linear stretch applied to combined TOPSAR Phv. All imagery is registered to GDA94 MGA Zone 55.

# 4 Conclusions

This study demonstrated the successful processing and application of TOPSAR DEM and associated multi –wavelength and –polarimetric data for geoscience information in western Tasmania. In particular, a preliminary examination of the higher resolution DEM product showed its potential as a  superior tool for topographic mapping and geological interpretation than available SRTM 25 imagery. A comparison of the TOPSAR DEM product with the 1:25,000 Tasmanian topographic mapping and other data sets revealed a high level of spatial and elevation accuracy. The DEM accuracy of the airborne TOPSAR data also appeared to provide consistent results, independent of the underlying geology. Although the terrain is generally forested with a variety of vegetation types, P band with a HV polarisation shows potential to map a range of surface roughness that may be related to geological units and their associated regolith. However it is recommended that the detailed 1:25,000 vegetation classification be used with any interpretation with this radar data. The complexity of radar scattering within rainforest canopies, vegetated understories and a damp regolith is likely to generate, at least partially, non-unique solutions to the question of geological versus vegetation controls. Also, an understanding of potential geobotanical associations and geologically defined variations in surface roughness would be further assisted with field work and ground truthing. Further processing of the TOPSAR data for estimates of effective layover distortion and radar shadowing using DEM information would also assist the interpretation.

# 5 Acknowledgements

This study has been kindly supported and funded by Mineral Resources Tasmania (MRT), with a considerable help from MRT's David Green. Professor Simon Jones of the School of Mathematical & Geospatial Sciences within RMIT University has also been supportive of this project. Technical assistance by Phil Wilkes, PhD candidate, has been forthcoming particularly in regard to handling LiDar data sets. Software support from Laurie Buxton of RMIT University was also helpful during this study.

# 6 References

Elachi, C. & Jakob J. van Zyl, J., (2006), "Introduction To The Physics and Techniques of Remote Sensing", 2nd Edition,John Wiley & Sons, New Jersey, ISBN: 978-0-471-47569-9.

ERDAS, (1999), "ERDAS Field Guide", Fifth Edition, ERDAS Inc., Atlanta, Georgia, http://www.gis.usu.edu/manuals/labbook/erdas/manuals/FieldGuide.pdf).

Evans, L., Farr, T.G., Van Zyl, J.J., and Zebker, H.A., (1988) , " Radar Polarimetry: Analysis Tools and Applications, *IEEE Transactions on Geoscience and Remote Sensing*, Vol. 26, No.6, pp. 774-789.

Ford, J.P., 1998, Radar Geology, in Principles and Application of Imaging Radar (F.M. Henderson and A.J. Lewis, eds.), Manual of Remote Sensing, Third Edition, Volume 2, John Wiley and Sons, Inc.

Hewson, R.D. and Taylor, G.R., (2000). "An investigation of the geological and geomorphological features of Fowlers Gap using thermal infrared, radar and airborne geophysical remote sensing techniques." *Rangeland Journal*, Vol. 22, pp. 105-123.

Huadong, G., Jingjuan, L., Changlin, W., Chao, W., Farr, T., Evans, D.L., (1996), "Use of Multifrequency, Multipolarisation Shuttle, Imaging Radar for Volcano mapping in the Kunlun Mountains of western China", *Remote Sensing of Environment*, Vol. 59, pp.364-374.

Kierein-Young, K.S., Kruse, F.A., and Lefkoff, A.B., (1992), "Quantitative Analysis of Surface Characteristics and Morphology in Death Valley, California, using AIRSAR data, *In Proc. Geoscience and Remote Sensing Symposium*, 2002, Houston, IEEE, pp. 392-394, DOI: 10.1109/IGARSS.1992.576720

Lee, Jong-Sen, "Digital Image Enhancement and Noise Filtering by Use of Local Statistics", (1980), *Pattern Analysis and Machine Intelligence*, *IEEE Transactions on Pattern Analysis and Machine Intelligence*, Volume: PAMI-2 , Issue: 2, pp 165-168.
DOI: 10.1109/TPAMI.1980.4766994

Lou, Yunling (2002), "Review of the NASA/JPL airborne synthetic aperture radar system," *In Proc. Geoscience and Remote Sensing Symposium*, 2002. IEEE, Vol. 3, pp. 1702 – 1704, DOI: 10.1109/IGARSS.2002.1026226

Lopes, A. ; Touzi, R. ; Nezry, E., (1990), "Adaptive speckle filters and scene heterogeneity", *IEEE Transactions on Geoscience and Remote Sensing*, Vol. 28 , No.6, pp. 992 – 1000. DOI: 10.1109/36.62623.

Madsen, S.N., Zebker, H.A., and Martin, J., (1993), "Topographic Mapping using Radar Interferometry: Processing Techniques," *IEEE Transactions on Geoscience and Remote Sensing*, Vol. 31, No. 1, pp. 246-256.

Raney, R.K., 1998, Radar fundamentals: technical perspective, in Principles and Application of Imaging Radar (F.M. Henderson and A.J. Lewis, eds.), Manual of Remote Sensing, Third Edition, Volume 2, John Wiley and Sons, Inc.

Tapley, I.J. (2002), "Radar Imaging" within "Geophysical and remote sensing methods for regolith exploration", Ed. Eva Pap, CRC LEME Open file report 144, http://crcleme.org.au/Pubs/OPEN%20FILE%20REPORTS/OFR%20144/05Radar.pdf

Zebker, H.A., Madsen, S.N., Martin, J., Wheeler, K.B., Miller, T., Lou, Yunling, Alberti, G., Vetrella, S. and Cucci, A., (1992), “The TOPSAR Interferometric Radar Topographic Mapping Instrument,” *IEEE Transactions on Geoscience and Remote Sensing*, Vol. 30 , No. 5, pp. 933 – 940.

# 7 Appendix 1

## Registration ground control points of TOPSAR imagery

Note : all imagery was registered to GDA94 MGA Zone 55.

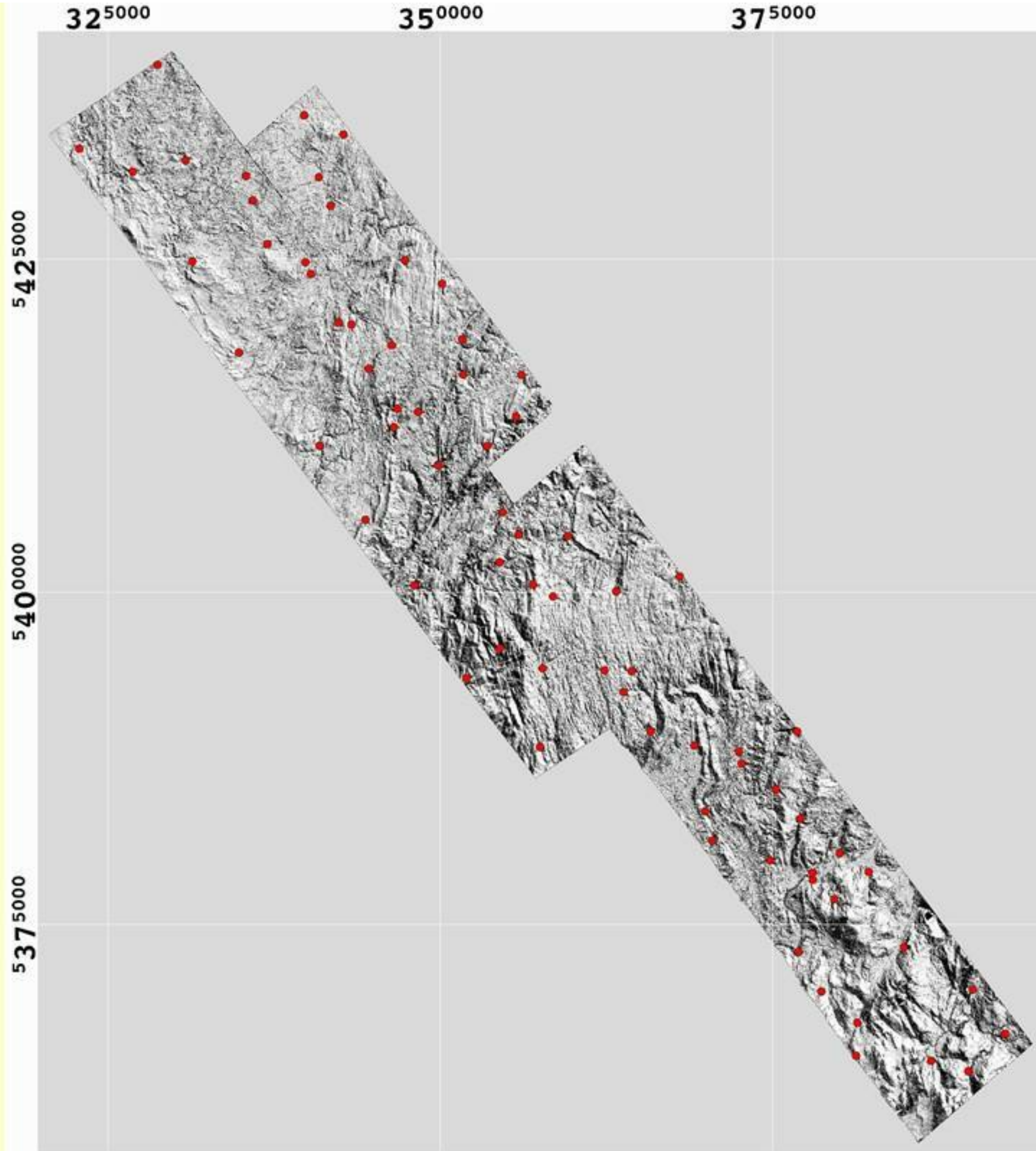


Figure A1 Shaded TOPSAR DEM with location of ground control points used for registration of each of the three TOPSAR flight lines, TS 1297, 1339 and 1340.

**TS1297 :**

```
; ENVI Image to Map GCP File
; projection info = {Geographic Lat/Lon, WGS-84, units=Degrees}
; warp file: C:\Tassie_MRT_AIRSAR-TOPSAR\ts1297\ts1297_c_dem_bad-value-remove
; Map (x,y), Image (x,y)
;
    145.73019400    -41.85010100       0.000000       0.000000
    145.61782800    -41.91090400    2284.000000       1.000000
    145.21191400    -41.49717700    2284.000000   11431.000000
    145.32418800    -41.43636300       0.000000   11431.000000
```

```
; ENVI Image to Map GCP File
; projection info = {3, 6378137.0, 6356752.3, 0.000000, 147.000000, 500000.0, 10000000.0, 0.999600, Geocentric Datum of Australia 1994, Map Grid of Australia (MGA 94) Zone 55, units=Meters}
; warp file: G:\Tassie_MRT_AIRSAR-TOPSAR\ts1297\ts1297_c_dem_bad-value-remove_MGA55_RST_shade45Az60El
; Map (x,y), Image (x,y)
;
    354469.7916   5402228.9750    621.000000   1920.000000
    364394.7916   5394028.9750   2688.000000   3540.000000
    377069.7916   5382953.9750   5305.000000   5721.000000
    376819.7916   5389503.9750   5263.000000   4404.000000
    372644.7916   5387078.9750   4390.000000   4886.000000
    370444.7916   5381303.9750   3940.000000   6062.000000
    359594.7916   5404203.9750   1698.000000   1516.000000
    379619.7916   5376903.9750   5838.000000   6915.000000
    382194.7916   5378953.9750   6365.000000   6500.000000
    384844.7916   5373278.9750   6923.000000   7625.000000
    363219.7916   5400028.9750   2440.000000   2332.000000
    365819.7916   5389528.9750   2980.000000   4435.000000
    369094.7916   5388453.9750   3655.000000   4638.000000
    375244.7916   5385153.9750   4931.000000   5288.000000
    380019.7916   5380378.9750   5911.000000   6232.000000
    374794.7916   5379803.9750   4839.000000   6351.000000
    377994.7916   5378353.9750   5502.000000   6630.000000
    378644.7916   5369953.9750   5648.000000   8301.000000
    381344.7916   5367628.9750   6189.000000   8776.000000
    390019.7916   5370103.9750   7990.000000   8263.000000
    392469.7916   5366803.9750   8480.000000   8907.000000
    389694.7916   5363978.9750   7915.000000   9478.000000
    381244.7916   5365153.9750   6175.000000   9257.000000
    386894.7916   5364753.9750   7329.000000   9310.000000
    356969.7916   5400528.9750   1139.000000   2255.000000
    362344.7916   5394103.9750   2251.000000   3521.000000
    367994.7916   5401178.9750   3430.000000   2089.000000
    377977.3770   5378879.3262   5494.000000   6524.000000
    376917.0650   5372954.3391   5271.000000   7703.000000
    355903.0313   5404300.5233    903.000000   1494.000000
    372451.9260   5388001.5225   4345.000000   4708.000000
    369902.5303   5383505.9756   3820.000000   5614.000000
```

Note : Root Mean Square (rms) error of registeration : 9.4 pixels

**TS1339 :**

; ENVI Image to Map GCP File
; projection info = {3, 6378137.0, 6356752.3, 0.000000, 147.000000, 500000.0, 10000000.0, 0.999600, Geocentric Datum of Australia 1994, Map Grid of Australia (MGA 94) Zone 55, units=Meters}
; warp file: C:\Tassie_MRT_AIRSAR-TOPSAR\ts1339\ts1339_c_demi2_convert_DEM_masked
; Map (x,y), Image (x,y)
;

| | | | |
|---|---|---|---|
| 320409.6464 | 5434507.1693 | 0.000000 | 0.000000 |
| 329478.6014 | 5441404.1975 | 2288.000000 | 1.000000 |
| 366965.1318 | 5392380.5798 | 2288.000000 | 12273.000000 |
| 357936.3988 | 5385527.6382 | 1.000000 | 12273.000000 |

; ENVI Image to Map GCP File
; projection info = {3, 6378137.0, 6356752.3, 0.000000, 147.000000, 500000.0, 10000000.0, 0.999600, Geocentric Datum of Australia 1994, Map Grid of Australia (MGA 94) Zone 55, units=Meters}
; warp file: G:\Tassie_MRT_AIRSAR-TOPSAR\ts1339\ts1339_c_demi2_convert_DEM_masked_MGA55_RST_Shade135Az60El
; Map (x,y), Image (x,y)
;

| | | | |
|---|---|---|---|
| 322869.7916 | 5433303.9750 | 511.000000 | 1748.000000 |
| 330869.7916 | 5432428.9750 | 2150.000000 | 1927.000000 |
| 328744.7916 | 5439603.9750 | 1703.000000 | 504.000000 |
| 331369.7916 | 5424828.9750 | 2276.120000 | 3448.160000 |
| 334870.0000 | 5417978.9750 | 2994.000000 | 4808.000000 |
| 342344.7916 | 5420228.9750 | 4526.000000 | 4350.000000 |
| 344616.4647 | 5416774.9417 | 4987.000000 | 5044.000000 |
| 340919.7916 | 5410978.9750 | 4255.000000 | 6207.000000 |
| 344394.7916 | 5405428.9750 | 4978.000000 | 7321.000000 |
| 349869.7916 | 5409503.9750 | 6078.000000 | 6498.000000 |
| 348069.7916 | 5400478.9750 | 5731.000000 | 8319.000000 |
| 354694.7916 | 5405978.9750 | 7073.000000 | 7223.000000 |
| 351969.7916 | 5393503.9750 | 6538.000000 | 9723.000000 |
| 358469.7916 | 5399653.9750 | 7863.000000 | 8486.000000 |
| 354469.7916 | 5395753.9750 | 7039.000000 | 9268.000000 |
| 357494.7916 | 5388328.9750 | 7670.000000 | 10752.000000 |
| 363794.7916 | 5392478.9750 | 8939.000000 | 9925.000000 |
| 357694.7916 | 5394253.9750 | 7703.000000 | 9563.000000 |
| 346519.7916 | 5412378.9750 | 5395.360000 | 5933.160000 |
| 335925.4663 | 5429417.0885 | 3188.640000 | 2522.540000 |
| 339866.1821 | 5424782.7668 | 4011.000000 | 3447.000000 |
| 326893.2004 | 5431585.2948 | 1337.000000 | 2089.000000 |

Note : Root Mean Square (rms) error of registeration : 7.3 pixels

**TS1340 :**

; ENVI Image to Map GCP File
; projection info = {Geographic Lat/Lon, WGS-84, units=Degrees}
; warp file: C:\Tassie_MRT_AIRSAR-TOPSAR\ts1340\ts1340_c-demi2_convert
; Map (x,y), Image (x,y)
;

| | | | |
|---|---|---|---|
| 145.31069900 | -41.41519900 | 1.000000 | 1.000000 |
| 145.20140100 | -41.47602800 | 2286.000000 | 1.000000 |
| 144.98007200 | -41.25043100 | 2286.000000 | 6234.000000 |
| 145.08926400 | -41.18959000 | 1.000000 | 6234.000000 |

; ENVI Image to Map GCP File
; projection info = {3, 6378137.0, 6356752.3, 0.000000, 147.000000, 500000.0, 10000000.0, 0.999600, Geocentric Datum of Australia 1994, Map Grid of Australia (MGA 94) Zone 55, units=Meters}
; warp file: C:\Tassie_MRT_AIRSAR-TOPSAR\ts1340\ts1340_c-demi2_convert_DEM-masked_MGA55_Shade_60El135Az
; Map (x,y), Image (x,y)
;

| | | | |
|---|---|---|---|
| 343319.7916 | 5420078.9750 | 2505.000000 | 3678.000000 |
| 347344.7916 | 5424928.9750 | 3300.000000 | 2704.000000 |
| 351644.7916 | 5418978.9750 | 4203.000000 | 3873.000000 |
| 349844.7916 | 5409553.9750 | 3875.000000 | 5757.000000 |
| 353519.7916 | 5410953.9750 | 4612.000000 | 5479.000000 |
| 355694.7916 | 5413178.9750 | 5045.000000 | 5033.000000 |
| 335929.0870 | 5429415.7599 | 964.000000 | 1830.000000 |
| 342740.8529 | 5434363.8219 | 2329.000000 | 824.000000 |
| 339771.1342 | 5435805.9494 | 1724.000000 | 545.000000 |
| 340282.2807 | 5423896.7677 | 1871.000000 | 2919.000000 |
| 341771.3644 | 5429013.9942 | 2155.000000 | 1893.000000 |
| 350144.7916 | 5423153.9750 | 3877.000000 | 3055.000000 |
| 348336.0057 | 5413514.2958 | 3547.000000 | 4971.000000 |
| 351723.9351 | 5416330.8849 | 4221.000000 | 4401.000000 |
| 356094.7916 | 5416303.9750 | 5114.000000 | 4402.000000 |
| 346769.7916 | 5413753.9750 | 3234.000000 | 4936.000000 |
| 335413.7162 | 5431249.0803 | 846.000000 | 1456.000000 |
| 336999.9600 | 5426133.9684 | 1190.170000 | 2478.550000 |
| 346344.7916 | 5418528.9750 | 3121.000000 | 3980.000000 |
| 340872.4542 | 5431167.4678 | 1962.000000 | 1466.000000 |

Note : Root Mean Square (rms) error of registeration : 4.8 pixels

# 7 Appendix 2

## Statistical comparison between DEM results from TOPSAR acquisitions

<u>TS1339 vs TS1340 :</u>

STATISTICS FOR DATASET: Tas_TOPSAR_DEM-1339_1340_intersected.ers
REGION: All

| | TS1339 | TS1340 |
|---|---|---|
| | ----- | ----- |
| **NullCells** | 104081846 | 104081846 |
| | | |
| **Non-NullCells** | 5164904 | 5164904 |
| **AreaInHectares** | 12912.26 | 12912.26 |
| **AreaInAcres** | 31906.892 | 31906.892 |
| | | |
| **Minimum** | 71.364 | 49.9 |
| **Maximum** | 555.983 | 719.514 |
| **Mean** | 319.281 | 320.428 |
| **Median** | 311.781 | 311.468 |
| **Std.Dev.** | 92.952 | 92.556 |
| **Std.Dev.(n-1)** | 92.952 | 92.556 |
| **Corr.Eigenval.** | 1.991 | 0.009 |
| **Cov.Eigenval.** | 17131.032 | 75.733 |

| **CorrelationMatrix** | TS1339 | TS1340 |
|---|---|---|
| **------------------** | ----- | ----- |
| **TS1339** | 1 | 0.991 |
| **TS1340** | 0.991 | 1 |
| **Determinant** | 0.018 | |

| **Corr.Eigenvectors** | PC1 | PC2 |
|---|---|---|
| **------------------** | ----- | ----- |
| **TS1339** | 0.707 | 0.707 |
| **TS1340** | 0.707 | -0.707 |

| **Inv.ofCorr.Ev.** | PC1 | PC2 |
|---|---|---|
| **-----------------** | ----- | ----- |
| **TS1339** | 0.707 | 0.707 |
| **TS1340** | 0.707 | -0.707 |

| CovarianceMatrix | TS1339 | TS1340 |
|---|---|---|
| ---------------- | ----- | ----- |
| **TS1339** | 8640.139 | 8527.57 |
| **TS1340** | 8527.57 | 8566.626 |
| **Determinant** | 1297392.466 | |

| Cov.Eigenvectors | PC1 | PC2 |
|---|---|---|
| ---------------- | ----- | ----- |
| **TS1339** | 0.709 | 0.706 |
| **TS1340** | 0.706 | -0.709 |

| Inv.ofCov.Ev. | PC1 | PC2 |
|---|---|---|
| --------------- | ----- | ----- |
| **TS1339** | 0.709 | 0.706 |
| **TS1340** | 0.706 | -0.709 |

TS1297 vs TS1339 :

STATISTICS FOR DATASET: Tas_TOPSAR_DEM-1297-1339_intersected.ers
REGION:All

| | TS1297 | TS1339 |
|---|---|---|
| | ----- | ----- |
| **NullCells** | 250922347 | 250922347 |
| **Non-NullCells** | 3200488 | 3200488 |
| **AreaInHectares** | 8001.43 | 8001.43 |
| **AreaInAcres** | 19771.965 | 19771.965 |
| **Minimum** | 4.619 | 128.584 |
| **Maximum** | 833.887 | 834.257 |
| **Mean** | 505.289 | 501.541 |
| **Median** | 542.347 | 542.064 |
| **Std.Dev.** | 132.846 | 135.511 |
| **Std.Dev.(n-1)** | 132.846 | 135.511 |
| **Corr.Eigenval.** | 1.995 | 0.005 |
| **Cov.Eigenval.** | 35916.763 | 94.498 |

| CorrelationMatrix | TS1297 | TS1339 |
|---|---|---|
| ----------------- | ----- | ----- |
| **TS1297** | 1 | 0.995 |
| **TS1339** | 0.995 | 1 |
| **Determinant** | 0.01 | |

| Corr.Eigenvectors | PC1 | PC2 |
|---|---|---|
| ----------------- | ----- | ----- |
| **TS1297** | 0.707 | 0.707 |

| | | |
|---|---|---|
| **TS1339** | 0.707 | -0.707 |

| **Inv.ofCorr.Ev.** | PC1 | PC2 |
|---|---|---|
| **TS1297** | 0.707 | 0.707 |
| **TS1339** | 0.707 | -0.707 |

| **CovarianceMatrix** | TS1297 | TS1339 |
|---|---|---|
| **TS1297** | 17648.111 | 17907.564 |
| **TS1339** | 17907.564 | 18363.15 |
| **Determinant** | 3394068.61 | |

| **Cov.Eigenvectors** | PC1 | PC2 |
|---|---|---|
| **TS1297** | 0.7 | -0.714 |
| **TS1339** | 0.714 | 0.7 |

| **Inv.ofCov.Ev.** | PC1 | PC2 |
|---|---|---|
| **TS1297** | 0.7 | 0.714 |
| **TS1339** | -0.714 | 0.7 |

# 7 Appendix 3

## Statistical comparison between DEM results from TOPSAR (TS1297), SRTM25m, Photogrammetric 25m and LiDar (Meredith)

STATISTICS FOR DATASET: Tas_DEM_analysis4b.ers
REGION: Meredith Granite

| | TOPSAR | SRTM25m | Photo25m | LiDAR |
|---|---|---|---|---|
| | ----- | ----- | ----- | ----- |
| **Null cells** | 75923 | 75923 | 75923 | 75923 |
| | | | | |
| **Non-Null cells** | 70578035 | 70578035 | 70578035 | 70578035 |
| **Area(Ha)** | 7057.863 | 7057.863 | 7057.863 | 7057.863 |
| **Area(acres)** | 17440.361 | 17440.361 | 17440.361 | 17440.361 |
| | | | | |
| **Minimum** | 309.724 | 322.547 | 313.056 | 312.168 |
| **Maximum** | 799.251 | 718.522 | 730 | 1160.635 |
| **Mean** | 564.214 | 562.759 | 562.079 | 561.317 |
| **Median** | 567.873 | 565.391 | 567.131 | 564.056 |
| **Std.Dev** | 48.533 | 48.441 | 51.048 | 51.886 |
| **Std.Dev(n-1)** | 48.533 | 48.441 | 51.048 | 51.886 |
| **Corr.Eigenval.** | 3.922 | 0.053 | 0.017 | 0.008 |
| **Cov.Eigenval.** | 9802.053 | 137.109 | 40.746 | 20.148 |

| **CorrelationEigenVector** | **TOPSAR** | **SRTM25m** | **Photo25m** | **LiDAR** |
|---|---|---|---|---|
| **-----------------** | ----- | ----- | ----- | ----- |
| **TOPSAR** | 1 | 0.984 | 0.984 | 0.953 |
| **SRTM25m** | 0.984 | 1 | 0.992 | 0.965 |
| **Photo25m** | 0.984 | 0.992 | 1 | 0.967 |
| **LiDAR** | 0.953 | 0.965 | 0.967 | 1 |
| **Determinant** | 0 | | | |

| **Corr.EigenVector** | PC1 | PC2 | PC3 | PC4 |
|---|---|---|---|---|
| **-----------------** | ----- | ----- | ----- | ----- |
| **TOPSAR** | 0.5 | -0.454 | 0.737 | -0.022 |
| **SRTM25m** | 0.502 | -0.211 | -0.491 | -0.68 |
| **Photo25m** | 0.503 | -0.173 | -0.425 | 0.733 |
| **LiDAR** | 0.495 | 0.848 | 0.186 | -0.032 |

| **Inv.** | PC1 | PC2 | PC3 | PC4 |
|---|---|---|---|---|
| **----------------** | ----- | ----- | ----- | ----- |
| **TOPSAR** | 0.5 | 0.502 | 0.503 | 0.495 |

| | | | | |
|---|---|---|---|---|
| **SRTM25m** | -0.454 | -0.211 | -0.173 | 0.848 |
| **Photo25m** | 0.737 | -0.491 | -0.425 | 0.186 |
| **LiDAR** | -0.022 | -0.68 | 0.733 | -0.032 |

| **Covariance** | **TOPSAR** | **SRTM25m** | **Photo25m** | **LiDAR** |
|---|---|---|---|---|
| **-----------------** | ----- | ----- | ----- | ----- |
| **TOPSAR** | 2355.497 | 2313.223 | 2438.293 | 2399.021 |
| **SRTM25m** | 2313.223 | 2346.567 | 2452.582 | 2424.755 |
| **Photo25m** | 2438.293 | 2452.582 | 2605.882 | 2560.855 |
| **LiDAR** | 2399.021 | 2424.755 | 2560.855 | 2692.11 |
| **Determinant** | 1103315978 | | | |

| **Cov.** | **TOPSAR** | **SRTM25m** | **Photo25m** | **LiDAR** |
|---|---|---|---|---|
| **-----------------** | ----- | ----- | ----- | ----- |
| **TOPSAR** | 0.485 | -0.446 | 0.752 | 0 |
| **SRTM25m** | 0.487 | -0.228 | -0.449 | -0.714 |
| **Photo25m** | 0.513 | -0.206 | -0.453 | 0.7 |
| **LiDAR** | 0.514 | 0.841 | 0.167 | -0.022 |

| **Inv.** | PC1 | PC2 | PC3 | PC4 |
|---|---|---|---|---|
| **----------------** | ----- | ----- | ----- | ----- |
| **TOPSAR** | 0.485 | 0.487 | 0.513 | 0.514 |
| **SRTM25m** | -0.446 | -0.228 | -0.206 | 0.841 |
| **Photo25m** | 0.752 | -0.449 | -0.453 | 0.167 |
| **LiDAR** | 0 | -0.714 | 0.7 | -0.022 |

STATISTICS FOR DATASET: Tas_DEM_analysis4b_no_Meredith.ers
REGION: No_Meredith_Granite

| | **TOPSAR** | **SRTM25m** | **Photo25m** | **LiDAR** |
|---|---|---|---|---|
| | ----- | ----- | ----- | ----- |
| **Non-NullCells** | 85406797 | 85406797 | 85406797 | 85406797 |
| **AreaInHectares** | 8540.752 | 8540.752 | 8540.752 | 8540.752 |
| **AreaInAcres** | 21104.66 | 21104.66 | 21104.66 | 21104.66 |
| **Minimum** | 3.531 | 105.086 | 97 | 94.982 |
| **Maximum** | 917.031 | 915.842 | 920 | 928.798 |
| **Mean** | 335.072 | 341.235 | 337.936 | 337.196 |
| **Median** | 321.115 | 326.777 | 318.824 | 319.721 |
| **Std.Dev.** | 160.957 | 159.243 | 160.217 | 159.258 |
| **Std.Dev.(n-1)** | 160.957 | 159.243 | 160.217 | 159.258 |
| **Corr.Eigenval.** | 3.995 | 0.003 | 0.001 | 0.001 |
| **Cov.Eigenval.** | 102182.685 | 69.109 | 29.725 | 16.677 |

| CorrelationMatrix | TOPSAR | SRTM25m | Photo25m | LiDAR |
|---|---|---|---|---|
| ------------------ | ----- | ----- | ----- | ----- |
| TOPSAR | 1 | 0.998 | 0.998 | 0.998 |
| SRTM25m | 0.998 | 1 | 0.999 | 0.999 |
| Photo25m | 0.998 | 0.999 | 1 | 0.999 |
| LiDAR | 0.998 | 0.999 | 0.999 | 1 |
| Determinant | 0 | | | |

| Corr.Eigenvectors | PC1 | PC2 | PC3 | PC4 |
|---|---|---|---|---|
| ------------------ | ----- | ----- | ----- | ----- |
| TOPSAR | 0.5 | -0.822 | -0.252 | -0.103 |
| SRTM25m | 0.5 | 0.028 | 0.86 | 0.102 |
| Photo25m | 0.5 | 0.334 | -0.384 | 0.701 |
| LiDAR | 0.5 | 0.46 | -0.223 | -0.699 |

| Inv.ofCorr.Ev. | PC1 | PC2 | PC3 | PC4 |
|---|---|---|---|---|
| ----------------- | ----- | ----- | ----- | ----- |
| TOPSAR | 0.5 | 0.5 | 0.5 | 0.5 |
| SRTM25m | -0.822 | 0.028 | 0.334 | 0.46 |
| Photo25m | -0.252 | 0.86 | -0.384 | -0.223 |
| LiDAR | -0.103 | 0.102 | 0.701 | -0.699 |

| CovarianceMatrix | TOPSAR | SRTM25m | Photo25m | LiDAR |
|---|---|---|---|---|
| ----------------- | ----- | ----- | ----- | ----- |
| TOPSAR | 25907.312 | 25587.659 | 25736.169 | 25574.251 |
| SRTM25m | 25587.659 | 25358.315 | 25484.135 | 25331.676 |
| Photo25m | 25736.169 | 25484.135 | 25669.439 | 25498.565 |
| LiDAR | 25574.251 | 25331.676 | 25498.565 | 25363.13 |
| Determinant | 3500760358 | | | |

| Cov.Eigenvectors | PC1 | PC2 | PC3 | PC4 |
|---|---|---|---|---|
| ----------------- | ----- | ----- | ----- | ----- |
| TOPSAR | 0.503 | -0.822 | -0.248 | -0.102 |
| SRTM25m | 0.498 | 0.033 | 0.86 | 0.105 |
| Photo25m | 0.501 | 0.337 | -0.388 | 0.697 |
| LiDAR | 0.498 | 0.459 | -0.22 | -0.702 |

| Inv.ofCov.Ev. | PC1 | PC2 | PC3 | PC4 |
|---|---|---|---|---|
| ---------------- | ----- | ----- | ----- | ----- |
| TOPSAR | 0.503 | 0.498 | 0.501 | 0.498 |
| SRTM25m | -0.822 | 0.033 | 0.337 | 0.459 |
| Photo25m | -0.248 | 0.86 | -0.388 | -0.22 |
| LiDAR | -0.102 | 0.105 | 0.697 | -0.702 |

REGION:All (Inc. Meredith & non-Meredith intrusives) :

| | TOPSAR | SRTM25m | Photo25m | LiDAR |
|---|---|---|---|---|
| | ----- | ----- | ----- | ----- |
| **NullCells** | 1206461396 | 1206461396 | 1206461396 | 1206461396 |
| | | | | |
| **Non-NullCells** | 176478100 | 176478100 | 176478100 | 176478100 |
| **AreaInHectares** | 17647.96 | 17647.96 | 17647.96 | 17647.96 |
| **AreaInAcres** | 43609.061 | 43609.061 | 43609.061 | 43609.061 |
| | | | | |
| **Minimum** | 3.531 | 102.597 | 97 | 94.982 |
| **Maximum** | 917.031 | 915.842 | 920 | 1160.635 |
| **Mean** | 434.5 | 437.099 | 434.686 | 434.036 |
| **Median** | 481.691 | 483.805 | 479.566 | 477.951 |
| **Std.Dev.** | 166.346 | 162.863 | 164.762 | 164.268 |
| **Std.Dev.(n-1)** | 166.346 | 162.863 | 164.762 | 164.268 |
| **Corr.Eigenval.** | 3.993 | 0.004 | 0.002 | 0.001 |
| **Cov.Eigenval.** | 108145.165 | 106.368 | 47.345 | 27.093 |

| **CorrelationMatrix** | TOPSAR | SRTM25m | Photo25m | LiDAR |
|---|---|---|---|---|
| **------------------** | ----- | ----- | ----- | ----- |
| **TOPSAR** | 1 | 0.998 | 0.998 | 0.996 |
| **SRTM25m** | 0.998 | 1 | 0.999 | 0.998 |
| **Photo25m** | 0.998 | 0.999 | 1 | 0.998 |
| **LiDAR** | 0.996 | 0.998 | 0.998 | 1 |
| **Determinant** | 0 | | | |

| **Corr.Eigenvectors** | PC1 | PC2 | PC3 | PC4 |
|---|---|---|---|---|
| **------------------** | ----- | ----- | ----- | ----- |
| **TOPSAR** | 0.5 | -0.748 | 0.435 | 0.042 |
| **SRTM25m** | 0.5 | -0.023 | -0.55 | -0.669 |
| **Photo25m** | 0.5 | 0.117 | -0.443 | 0.734 |
| **LiDAR** | 0.5 | 0.653 | 0.558 | -0.108 |

| **Inv.ofCorr.Ev.** | PC1 | PC2 | PC3 | PC4 |
|---|---|---|---|---|
| **-----------------** | ----- | ----- | ----- | ----- |
| **TOPSAR** | 0.5 | 0.5 | 0.5 | 0.5 |
| **SRTM25m** | -0.748 | -0.023 | 0.117 | 0.653 |
| **Photo25m** | 0.435 | -0.55 | -0.443 | 0.558 |
| **LiDAR** | 0.042 | -0.669 | 0.734 | -0.108 |

| **CovarianceMatrix** | TOPSAR | SRTM25m | Photo25m | LiDAR |
|---|---|---|---|---|
| **-----------------** | ----- | ----- | ----- | ----- |
| **TOPSAR** | 27670.998 | 27033.976 | 27342.512 | 27220.512 |
| **SRTM25m** | 27033.976 | 26524.266 | 26805.697 | 26696.373 |

| | | | | |
|---|---|---|---|---|
| **Photo25m** | 27342.512 | 26805.697 | 27146.611 | 27016.629 |
| **LiDAR** | 27220.512 | 26696.373 | 27016.629 | 26984.095 |
| **Determinant** | 14755001395 | | | |

| **Cov.Eigenvectors** | PC1 | PC2 | PC3 | PC4 |
|---|---|---|---|---|
| **-----------------** | ----- | ----- | ----- | ----- |
| **TOPSAR** | 0.505 | -0.75 | 0.424 | 0.046 |
| **SRTM25m** | 0.495 | -0.014 | -0.542 | -0.679 |
| **Photo25m** | 0.501 | 0.124 | -0.455 | 0.726 |
| **LiDAR** | 0.499 | 0.649 | 0.565 | -0.101 |

| **Inv.ofCov.Ev.** | PC1 | PC2 | PC3 | PC4 |
|---|---|---|---|---|
| **----------------** | ----- | ----- | ----- | ----- |
| **TOPSAR** | 0.505 | 0.495 | 0.501 | 0.499 |
| **SRTM25m** | -0.75 | -0.014 | 0.124 | 0.649 |
| **Photo25m** | 0.424 | -0.542 | -0.455 | 0.565 |
| **LiDAR** | 0.046 | -0.679 | 0.726 | -0.101 |